Beta Titanium Alloys Processed By Laser Powder Bed Fusion: A Review

J.C. Colombo-Pulgarín ⬤, C.A. Biffi, M. Vedani, D. Celentano, A. Sánchez-Egea, A.D. Boccardo, and J.-P. Ponthot

In βTi-alloys, some advances and developments have been reached toward optimizing their mechanical performance and their processability. However, the applications of these alloys via laser powder bed fusion (LPBF) are still under investigation. In this work, the processing of βTi-alloys via LPBF and their properties is reviewed with a focus on six selected metallurgical systems which are expected to be top performance materials in applications in the aeronautical and biomedical contexts. These six systems promise a better mechanical and functional performance considering different in-service environments for medical implants and structural applications. After literature analysis, the applicability of βTi-alloys to be processed via LPBF is then discussed considering the relevant fields of applications.

Keywords	beta titanium alloys, laser powder bed fusion, mechanical behavior, microstructure, processability

Abbreviations	
AER	Aeronautic
AlE	Aluminum equivalency
ALMT	Additive Layer Manufacturing Technologies
AM	Additive manufacturing
BASCA	Beta anneal slow cool age
BCC	Body-centered cubic
BIO	Biomedical
CC	Critical concentration
CP-Ti	Commercially pure titanium
FCC	Face-centered cubic
EPBF	Electron powder bed fusion
HAZ	Heat-affected zone
HCP	Hexagonal close packed
LPBF	Laser powder bed fusion
MoE	Molybdenum equivalency
OTiA	Orthorhombic titanium alloys
OR	Orientation relationship
PBF	Powder bed fusion
SE	Stabilizing elements
STA	Solution treatment and aging
STOA	Solution-treated and overaged
TGM	Temperature gradient mechanism.
Ti-alloys	Titanium alloys

List of Symbols

S_y	Yield strength.
T_β	Beta transus temperature

1. Introduction

Powder bed fusion (PBF) processes belong to the Additive Layer Manufacturing Technologies (ALMT) category in which an object is produced by the sequential addition of material

J.C. Colombo-Pulgarín, Department of Mechanical Engineering, Politecnico di Milano, Piazza Leonardo Da Vinci 32, Milan, Italy; Department of Mechanical and Metallurgical Engineering, Engineering School. Pontificia, Universidad Católica de Chile, Vicuña Mackenna 4860, Santiago, Chile; and Institute of Condensed Matter Chemistry and Technologies for Energy, Unit of Lecco, CNR ICMATE, National Research Council, Via Previati 1/E, 23900 Lecco, Italy; **C.A. Biffi**, Institute of Condensed Matter Chemistry and Technologies for Energy, Unit of Lecco, CNR ICMATE, National Research Council, Via Previati 1/E, 23900 Lecco, Italy; **M. Vedani**, Department of Mechanical Engineering, Politecnico di Milano, Piazza Leonardo Da Vinci 32, Milan, Italy; **D. Celentano**, Department of Mechanical and Metallurgical Engineering, Engineering School. Pontificia, Universidad Católica de Chile, Vicuña Mackenna 4860, Santiago, Chile; **A. Sánchez-Egea**, Department of Mechanical Engineering, Universitat Politècnica de Catalunya, C. Jordi Girona, 1-3, 08034 Barcelona, Spain; **A.D. Boccardo**, Mechanical Engineering, School of Engineering, College of Science and Engineering, NUI Galway, University Road, Galway H91 HX31, Ireland; I-Form Advanced Manufacturing Research Centre, NUI Galway, University Road, Galway H91 HX31, Ireland; and Instituto de Estudios Avanzados en Ingeniería y Tecnología, IDIT, CONICET-Universidad Nacional de Córdoba, Vélez Sarsfield 1611, X5000 Córdoba, Argentina; and **J.-P. Ponthot**, Département d'Aerospatiale et Mecanique/LTAS-MN2L, Universite de Liège, Allée de la Decouverte 13A, 4000 Liège, Belgique. Contact e-mails: jccolombo@uc.cl and juancamilo.colombo@polimi.it.

layers following instructions based on data of a CAD file previously conceived. In PBF processes, a laser beam or an electron beam can be used as energy sources for thermal processing the material layers which generate the object until the desired shape is reached. These two energy sources characterize two different processes: laser powder bed fusion (LPBF) and electron powder bed fusion (EPBF) processes. These two processes allow generating metallic objects from

layer-by-layer thermal processing. The metal powder particles are heated up to melt by the resultant action of the interaction with the energy source, either photons from the laser beam or electrons from the electron beam. After melting, the thermally affected volume of material solidifies. The energy source/material interaction occurs along different tracks in the same layer which in turn is experienced sequentially in subsequent layers. It configures thermal cycles which act on the material domain in such a way that different metallurgical, chemical and physical phenomena are expected to occur-in different time scales-which affect the final microstructure and functional properties of the produced object. The starting powdered material is physically contained in the powder bed volume from which the final component is generated after the layers addition sequence is completed. The powder bed is the material domain of the metal powder particles from which new solid material layers are generated.

As mentioned above, a laser beam is used as a thermal source for heating up the powdered material when processed via LPBF. During the LPBF process, a stream of photons impacts on a focal point on the powder bed and such collision with the surface of particles produces enough heat to change the physical state and the microstructural features of the particle. Besides impacting on the powder bed surface, the laser beam penetrates it, so repeated reflections between underlying neighboring particles may happen (Ref 1, 2). Following a path previously defined and setup, the laser scans the current layer until completed. Later, a subsequent layer is deposited—after building, the platform lowers a distance equal to the layer thickness—by spreading with a roller a new powdered material layer and thermally processed. The process is cyclically repeated until completing the final geometry of the object. LPBF is a process in which the material and part are both created simultaneously (Ref 3, 4). As a result of the process and the repeated thermal cycles, the being-processed material experiences repeated solid-state and liquid–solid-phase transformations. It leads to microstructural changes which affect the mechanical properties of the material. Establishing trends and relationships between them is difficult because there are influences between most of those features with each other (Ref 5). An important concern in the LPBF process is how the material microstructure evolves. It implies that both the energy density and heat transferred by the laser interact with the material crystal lattice. This interaction is reflected in time-dependent temperature profiles experienced by materials when the feedstock to be thermally processed is subjected to the laser beam effect (Ref 6-8). The LPBF process can be compared to a repetitive welding process in which thousands of welds are stacked next to and on top of each other to produce a 3D geometric domain. The main difference is that the purpose of welds is to join two or more separate geometries into one, while in the LPBF process the welds themselves are the geometry. In LPBF, the molten pool dimensions are in the order of 0.1 mm^3 that is related to the scale in which the process takes place as compared to the welding process.

Upon processing Ti-alloys via LPBF, the final microstructure is dependent on the thermal history, processing parameters and how they interact with each other. Besides the tailorable microstructure that can be achieved by tuning optimal processing conditions in LPBF, the inherent features and attributes of βTi-alloys allow satisfying the requirements and specifications from industries as diverse as biomedical, petrochemical, aerospace and power generation. Their functional versatility is related to good corrosion resistance, high mechanical strength and ease of fabrication as compared to other Ti-alloys (Ref 9). Volume fraction variations can be performed in some specific compositions for adjusting the elastic modulus to make it appropriate for biomedical applications. Structural applications in aerospace are among the most promising approaches to be used because of low weight components that can be manufactured by keeping outstanding corrosion resistance and mechanical performance under fatigue load regimes and load-bearing applications.

The aim of this work is to provide a comprehensive review of the processing, microstructure and properties of six metallurgical systems of βTi-alloys processed by LPBF, selected as potential representative materials to be used in biomedical and aeronautical applications. Some of these compositions have already been tested for LPBF. However, the research results obtained until now are relatively scarce in terms of understanding of mechanical response and additive manufacturing processability. The importance of these six compositions—which makes them attractive for being analyzed in this review—lies in their promising performance in aeronautical and biomedical applications as compared to the most-used composition of the Ti64 alloy. Conclusions are finally drawn, suggesting the next challenges aimed at widening the applicability of βTi-alloys in their relevant fields when processed via LPBF.

2. Material Consolidation in LPBF

For a complete powdered material consolidation, the laser energy—carried by photons as quantum of light—must be absorbed in such amount that the irradiated material in the powder bed heats up enough for reaching the melting temperature. The absorption of the laser energy on the scanned powder bed produces rapid heating—after the laser energy transforms into thermal energy—that raises the local temperature to above the material melting temperature. The heating up of powder particles occurs rapidly at rates in the range of 10^3 to 10^8 K/s in very short time periods (Ref 10, 11). The relative density and reflectivity of the powder particles determine the thermal energy distribution inside of the powder bed under the top powdered layer. After that, the temperature decreases locally, and the molten material solidifies to form a solid material domain. Material shrinkage as it solidifies induces stresses in the surrounding material which can partially relax when successive layers are deposited. The solidification is carried out at high cooling rates because of thermal cycles when the heat source transfers its energy on small-sized molten pools and moves on.

The thermal cycles are referred to the numerous reheating and recooling processes that happen when upcoming layers are deposited, even in the same layer after thermal tracks are drawn continuously based on the scanning strategy. The high heating and cooling rates are one of the key inherent features of the LPBF process. This sequence of thermal phenomena makes the LPBF process to be very dynamically active and kinetically unstable and leads to produce metastable microstructures and non-equilibrium compositions of the resulting phases. These microstructures and their stoichiometric compositions may vary for each layer of the deposited material (Ref 7). The surrounded material—as both solidified mass and loose powder—also

plays an important role in the material consolidation phenomena. Slight thermal variations may occur during the laser scans because of surrounding cold powder particles. The presence of solidified surrounded mass may also modify the heat flow as it improves when the material density increases (Ref 12, 13).

In the LPBF process, the fusion of the powdered material occurs by a raster motion of the laser heat source using galvanometer driven mirrors, resulting in melting and solidification of overlapping molten tracks. The use of laser allows controlled melting and solidification in the process resulting in good dimensional accuracy and surface finish. The factors contributing to surface quality include alloy type, powder morphology, size and shape, laser beam focal spot size and other process and design parameters. During LPBF, the absorption of the thermal energy by the material affects hierarchically the temperature profiles, molten pool geometry, solidification process, microstructure and functional properties of the printed part. The energy absorption depends on the heat source characteristics such as total power, profile and distribution of the heat source, radius of the heat source and radial distance of any point from the axis. The power density distribution of heat sources like lasers, electron beams and plasma arcs follow axisymmetric Gaussian profiles (Ref 14). LPBF has more similarities with welding than casting. LPBF and welding processes share important physical and metallurgical features like the moving heat source and the formation of a fusion zone with recirculating liquid metal that travels along with the heat source. However, scanning speeds and heat source powers are very different. Figure 1 shows such similarities between the two processes.

The kinetic and dynamic events inside the molten pool are dominated by convective phenomena, among others. The liquid metal is mixed by the convective flow coming from different regions. It enhances the transport of heat within the molten pool. The molten pool shape and dimensions depend on the amount of heat supplied not only by the heat source but also by the heat transfer and flow of the molten metal within the liquid pool. The shape changes severely due to coalescence and the movement induced by surface tension (Ref 4, 14). The temperature distribution in the liquid alloy, heating and cooling rates, solidification pattern, microstructure and final properties of the printed part are strongly affected by the circulation pattern. The process itself is controlled by the selected scanning strategy (Ref 10, 14, 16). The cooling of the molten pool is accomplished mainly by the conduction of heat through the part and the substrate. Depending on the substrate temperature and laser energy density, the cooling rate at the solid–liquid interface varies from 10^3 to 10^8 K/s (Ref 4, 10). If it were possible, changes in these heating rates would allow a wider control of the final microstructures and properties of LPBF printed parts, but it is not easy to achieve this in situ.

The local solidification growth rate, R (mm/s), and the temperature gradient, G (K/mm), at the solid–liquid interface are the two most important thermal parameters that affect the final solidification structure and consolidation of the powdered material processed via LPBF. The morphology of the solidification structure is affected by the ratio (G/R). While the cooling rate $(G \cdot R)$ affects the scale of the microstructure, G and R are both affected by the shape of the fusion zone and the temperature field (Ref 14). The interaction between R and G and their effect on the solidification microstructure can be schematically observed in the solidification map of Fig. 2.

Based on what is shown in Fig. 2, the dimensions of the solidification microstructures (planar, cellular, columnar dendritic and equiaxed dendritic) decrease as the cooling rate $(G \cdot R)$ increases. Higher cooling rates mean finer microstructures. These solidification maps can be used in some Ti-alloys for predicting which microstructures will be formed during solidification. Generally, the most widely observed solidification microstructures in metal components processed via LPBF are columnar and equiaxed structures (at high solidification growth rates and low thermal gradients) (Ref 14). The rapid heating and cooling of the LPBF process lead to sharp peaks in time–temperature plots that result in steep slopes, which mean high heating and cooling rates. The progressive increment in the baseline of the plot is related to the thermal energy accumulation as the heat source moves on the scanning domain of the current material layer, as it is shown in Fig. 3.
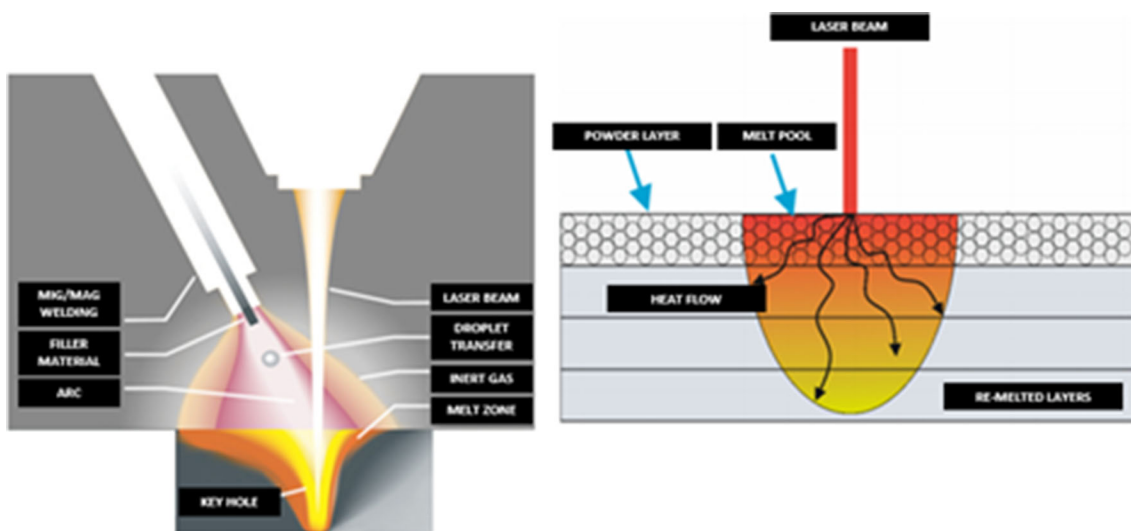

Fig. 1. On the left, main variables of the laser welding process. On the right, main variables of the LPBF process (Ref 15)
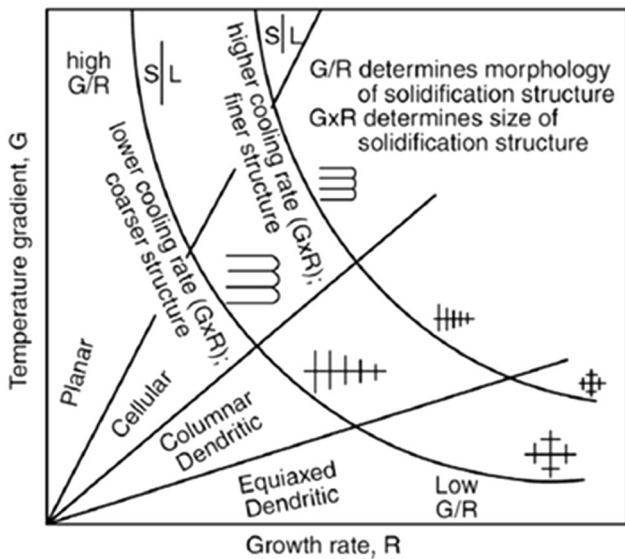
Fig. 2. Effect of temperature gradient and growth rate on the morphology and size of the solidification microstructure. Reprinted from Ref 14, Copyright 2018, with permission from Elsevier
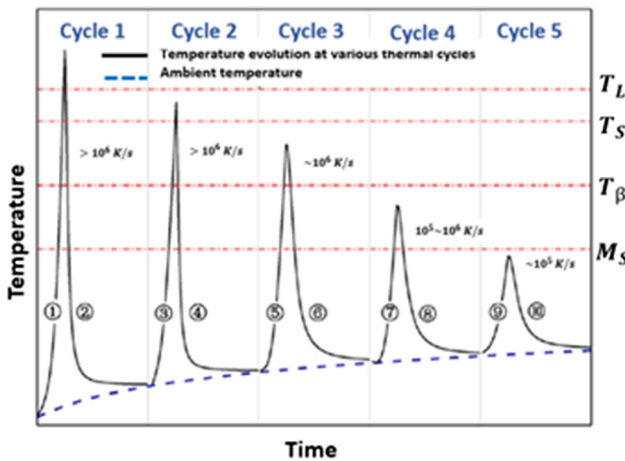

Fig. 3. Schematic diagrams illustrating types of LPBF thermal cycles. Reprinted from Ref 17, Copyright 2016, with permission from Elsevier

For instance, using the early stage of the heat cycle in Ti64, the primary and secondary α'-martensite laths at the microsized level seem to nucleate and grow. After some thermal cycles, further growing can be detected. On the other hand, tertiary and quartic α'-martensites are believed to be formed during the later stage of the heat cycle, as shown in Fig. 4 (Ref 17).

Although the local control of the solidification microstructures is desirable in LPBF, this is difficult to be practically achieved due to the speed at which thermal and metallurgical phenomena happen. Thus, one possible strategy is to try to manipulate G and R during the process in such a way that both solid-to-solid and solid-to-liquid transformations—which often occur during the process from track to track and layer to layer—are conducted upon convenience for the desired mechanical behavior. In practice, numerical simulation results could provide approximate information on what could be expected considering all the restrictions and idealizations that need to be defined in the simulation context (Ref 18-20).

3. Lattice Structures of Titanium Alloys

Lattice structures [also related to hierarchical architected materials, trabecular structures and metamaterials (Ref 21-23)] are obtained by using a regular pattern of struts and nodes. Fundamentally, these kinds of structures contain material voids which provide significant functional and structural advantages according to the final application. The versatility of the LPBF process allows building unconventional geometries like lattice structures. The overall performance of a based-on-lattice-structure component is basically governed by the microarchitecture of the lattice domain (Ref 24). A relevant target in lattice structures design is topology optimization with regard to applications such as energy absorption, type of mechanical response (bending-dominated, stretching-dominated, etc.), among others (Ref 21, 22, 24). For instance, structural lightness, strongness and stiffness are considered as key features in biomedical and aerospace applications for which lattice structures can provide these properties.

In the work of Ref 25, two optimized topology designs were analyzed both experimentally and numerically. Outstanding strength and stiffness-to-weight ratios were demonstrated to be obtained by using topology optimization. Focused on the high specific strength of the optimized structure, the finite element analysis disclosed the efficiency of its design. Besides, the results leave an open path toward strengthening the theory of porous strength and a stronger design of topology optimized structures. Lattice structures design must consider energy absorption as a key consideration. Moreover, the work performed in Ref 26 studied three porous structures for evaluating the energy absorption mechanisms at the early stage of deformation. The differences in local stress concentration and the stress distribution in the structures were found to be responsible for the different energy absorption mechanisms. One of the evaluated structure was found to have a high energy absorption ability which makes it an excellent candidate in the biomedical field for implant applications (Ref 23).

Intrinsic physical features like porosity are highly influenced by their random distribution and variation in size and orientation. The results obtained in Ref 27 showed the effect on super-elastic property, compressive strength, fatigue properties and Young's modulus of the porosity variation of structures of Ti2448 processed via EPBF. By increasing the porosity, an improvement of the superelastic property was found as a result of increasing the tensile/compressive stress ratio. By comparing with Ti64 (Ref 28, 29), the processing of Ti2448 via EPBF results in a higher normalized fatigue strength owing to the superelastic property and the larger plastic zone found around the crack tip (Ref 30). Similar to Ref 27, porous structures of Ti2448 processed via EPBF were also studied by Liu et al. (Ref 31) evaluating similar ranges of porosity values. Stronger struts and fewer defects were found by using lower electron beam scan speed. The optimal results found from such processing conditions allowed to observe better mechanical properties and at least twice the strength-to-modulus ratio of Ti64 porous components with the same level of porosity. The precipitation of α phase at β grain boundaries due to high-temperature preheating is believed to be responsible of such excellent properties. A work of functionally graded meshes produced via EPBF was reported in Ref 32. Similar to Ref 27, compressive and fatigue behavior of such meshes were both studied through the analysis of fundamental mechanisms that
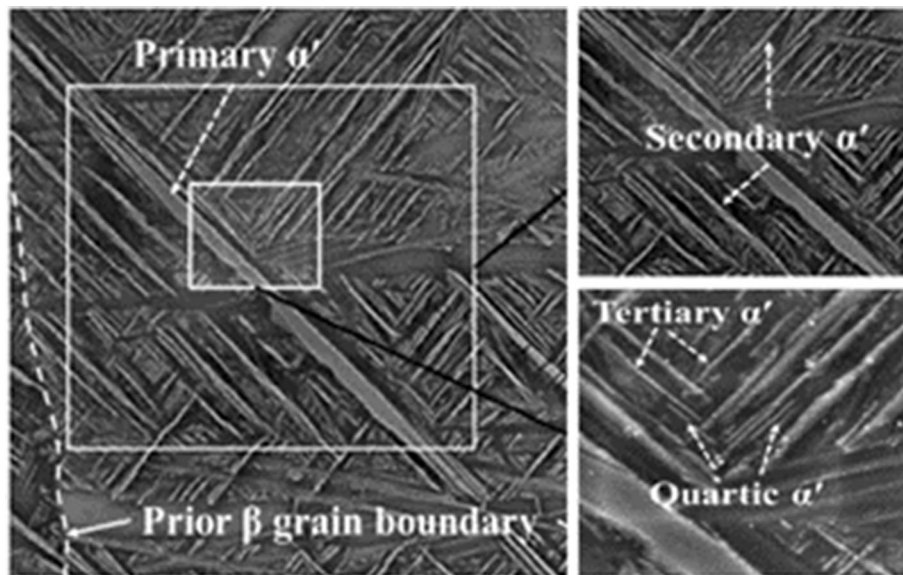
Fig. 4. SEM images of α′-martensites in Ti64 processed via LPBF. Reprinted from Ref 17, Copyright 2016, with permission from Elsevier

govern both mechanical conditions. The cracks initiation and propagation in the constituent meshes were both detected to start upon increasing the fatigue cycles from high to low strength until failure of the graded meshes. This was observed to be a progressive tendency. By considering a lower strength scenario, the propagation of cracks in meshes with higher strength was observed to be related. A good combination of high energy absorption, high fatigue strength and low density was observed to happen through an appropriate design of the constituent unit cells.

A comparison between CP-Ti and Ti64 was performed in Ref 33 in which two different topology optimized lattice structures were analyzed in terms of their fatigue properties. Upon investigating the effect of the shape of the unit cell on the fatigue properties and stress distribution, an enhancement in the plasticity was found through a reduction of stress concentration on the strut and twinning on the topology optimized CP-Ti structure occurring during the cycle deformation. This structure also showed highly normalized fatigue life which was mainly attributed to the combination of the high ductility of the material and a uniform stress distribution. There were also found samples of CP-Ti that contain specific twins which increase their ductility.

As mentioned before, the aeronautical and biomedical fields are a target for the applications of the six metallurgical systems discussed in the next section. Besides, lattice structures provide structural stability and high mechanical performance in both aeronautical and biomedical applications. Specifically, in the aeronautical field, different kind of components have so far been able to be manufactured via different metal additive manufacturing technologies and put into service. GE Aviation, Rolls-Royce, BAE Systems and Lockheed Martin are among the main aircraft part manufacturers currently applying LPBF for producing components and provide them to the main aircraft producers like Airbus and Boeing. Every service provider, component supplier and designer, and aircraft manufacturer have had to properly certified their production processes in order to fulfill the high-level quality requested by the aircraft industry according to its stringent standards. Some advantages, like low lead times and production costs,

lightness in weight and easy of assembly, are among the great achievements in the aeronautical field upon using metal AM (Ref 34). Direct conversion of raw materials into complex 3D geometries as from a digital CAD file generated in a previous design and product development stage allows significant time and cost savings where metal AM technology is suitable for producing final use parts. Considering the inventory and supply chain constraints, and the need for satisfying the just-in-time manufacturing, metal AM is particularly interesting in the aircraft industry because of its ability to make the raw material conversion as described above, without the need of elaborating tooling (Ref 35, 36).

In the biomedical field, important achievements like high osseointegration and a better grip of living tissues can be highlighted because of the use of porous and lattice structures produced via LPBF. This kind of structures stimulate the natural growing and time evolution of muscles and inner biological structures covering prosthesis or biomedical implants thank its similarity with bones topology. Weight lightness of implants produced via LPBF is also an advantage because patients are less prone to over stress or fatigue upon moving their body part carrying the implant (Ref 37). An adequate combination of high biocompatility, low density, low Young's modulus, good fatigue resistance and good corrosion resistance is required by a material for being adequate on biomedical applications. Upon processing via LPBF, it is important to obtain full density and defect-free parts. It is not an easy goal to be fulfilled because the process itself does not imply a mechanical pressure constantly acting. On the contrary, gravity and capillary forces act during the powder consolidation process influenced also by the thermal effects. As a general rule, CP-Ti and its alloys exhibit low hardness and wear properties. It is detrimental for their applications in the biomedical field especially when the combination of high strength and wear resistance is unavoidable needed. Therefore, biocompatible adding compounds like TiB_2 can be used for reinforcement of Ti-based compositions and for improving their wear properties (Ref 38).

Processing of Ti-alloys via LPBF is highly influenced by intrinsic process parameters like energy density, layer thickness

and scanning strategy, and also by inherent powder parameters like particles morphology and size distribution (Ref 39, 40). Based on the laser processing parameters, the microstructural features of CP-Ti vary from platelike α to acicular martensitic α′. At relatively low scan speed values and constant energy density, complete allotropic transformation β to α occurs upon solidification. As it is well known, the mechanical properties like tensile strength and hardness of CP-Ti are positively affected as compared to those produced by conventional manufacturing methods. In general terms, the mechanical properties reached upon LPBF processing of some Ti-alloys like Ti2448 are close to those of human bones. This aspect makes it a suitable Ti composition for applications on bone implant and implanted prosthesis (Ref 41, 42). Stainless steels are less commonly used in biomedical applications. However, their excellent combined properties of low elastic modulus, high specific strength, excellent corrosion resistance and superior biocompatibility makes them a good option for manufacturing biomedical implants. Similar functional and mechanical features have Co-Cr based alloys (Ref 42). Ti-alloys like (α + β)-type compositions (e.g., Ti64) exhibit better mechanical properties and have also been used for orthopedic implants. However, their moduli are significantly higher than those of bones and contain harmful elements like V and Al. The mismatch between implant and bone moduli generates the effect called stress shielding, which produces a reduction in the density of bone close to the implant that is not desired because it is obtained an implant–bone bond with low mechanical properties.

The easy of functionality and life or human limbs or joints are function of the mechanical properties that are considered as core (Young's modulus, tensile/compressive strength, toughness) when designing biomedical implants. These have been found to be function of age, location in the body, gender and disease history. The influence of features like pore size and its structure has been studied in Ref 43. A significant effect was found in the cell culture results in terms of a recommended interconnection for the improvement of the bone formation rate and also for an adequate implant fixation. The roughness of the surfaces was also analyzed in terms of osseointegration once the implant was placed and how the surrounding biological tissues interact with it.

4. Beta Phase Titanium Alloys

A Ti-alloy is considered as a βTi-alloy when the β-phase is substantially retained, under equilibrium or at least upon quenching from 100% β-phase field without transformation to martensite or α-phase. Enough amount of β-phase stabilizing elements causes a high strength up to 1400 MPa after a heat treatment (Ref 44, 45). Heat treatments can be used for improving the mechanical properties of these alloys. Solution treatment and aging (STA) is the most common heat treatment applied on β-phase Ti-alloys. STA is done above T_β as a regular process.

Some specific heat treatments were thought for specific compositions. Beta anneal slow cool age (BASCA) is a heat treatment applied on Ti5553 manufactured components for improving their mechanical strength. On the other hand, solution-treated and overaged (STOA) is a heat treatment applied on Beta 21S alloy. This treatment is used to increase the strength moderately while maintaining satisfactory toughness and dimensional stability. The Alloy C, which is one of the compositions analyzed in this review, can be annealed to improve the ductility, and refine the grain structure. The cooling method will depend on the desired properties (Ref 35, 46).

Room-temperature yield strength S_y of the βTi-alloys is significantly higher than those of other Ti-alloys. Good forming capability due to the presence of the β-phase, among other types of Ti-alloys, leads to easier cold rolling of βTi-alloys (Ref 9). However, βTi-alloys are not weldable and their creep resistance is lower with respect to that of αTi-alloys (Ref 47, 48). The strength S_y of most βTi-alloys is between 1150 and 1300 MPa, which is greater than that of αTi-alloys (750-1000 MPa) (Ref 48). The elastic modulus and strength of βTi-alloys can be affected by the formation or the absence of the ω-phase. Therefore, it is important to understand the formation mechanism of the ω-phase in the β-phase to identify alloying elements that can suppress or facilitate the ω-phase formation (Ref 49). This phase may form during quenching from the single β-phase field to room temperature with a hexagonal—not closed packed—crystallographic structure at small concentrations of β-phase stabilizing elements. At greater concentrations of them, the crystallographic structure is trigonal (Ref 9).

In this review, six metallurgical systems of βTi-alloys are analyzed in terms of processing, phase transformation, microstructure and mechanical behavior. Four of those systems are among the small selected group of aerospace alloys in current production. The two other are β-phase Ti-alloys highly attractive for biomedical applications because of their features related to Young's modulus, mechanical strength and biocompatibility.

The advantages of βTi-alloys include their high strength, good corrosion resistance, excellent biocompatibility and ease of fabrication compared to other high-performance alloys (Ref 9). In some specific cases, partial or total superelasticity can also be part of their features, which becomes attractive for biomedical applications (Ref 50, 51). Some other reference compositions of βTi-alloys that feature the advantages and disadvantages of Table 1 are Ti-11.5Mo-6Zr-4.5Sn, Ti-29Nb-13Ta-4.6Zr, Ti-13V-11Cr-3Al, Ti-30Mo, Ti-40Mo.

New low modulus βTi-alloys are being developed for biomedical applications. One of the challenges to be overcome is the inhomogeneity in the stress transfer between the medical implant and bone. The inhibition of bone atrophy is the main goal of the new compositions for this kind of application (Ref 52, 53). Reduction of Young's modulus is of considerable importance in biomedical applications to prevent stress shielding that induces bone resorption (i.e., the reabsorption of the bone tissue, which affects the mechanical response of the bone) and bone loosening (Ref 31, 54). By generation of different textures and controlling the growth behavior of columnar cells, suppressing stress shielding can potentially be achieved (Ref 55). Despite the high potential of βTi-alloys, these alloys have not been extensively investigated to be processed via LPBF due to the lack of availability of these compositions as powders. This fact reveals the opportunity for delving into their processability via LPBF.

The phase transformation of β-phase in Ti-alloys depends on the β-phase SE, such as Nb, V, Mo, Ta, Mn and Fe. The phase transformations from β to α″, α′ and ω phases upon quenching can be adjusted by controlling the content of the SE in the parent β-phase. The multifunctional properties of these alloys

Table 1 Advantages and disadvantages of β-phase Ti-alloys (Ref 44)

Advantages	Disadvantages
High strength-to-density ratio	High density
Low modulus (biomedical applications)	Low modulus (structural applications)
High strength/high toughness	Poor low- and high-temperature properties
High fatigue strength	Small processing window (some alloys)
Good deep hardenability	High formulation cost
Low forging temperature	Segregation problems
Strip producible—low-cost thermomechanical processing (some alloys)	High springback
Cold formable (some alloys)	Microstructural instabilities
Excellent corrosion resistance (some alloys)	Poor corrosion resistance (some alloys)
Easy to heat treat	Interstitial elements pick up
Excellent combustion resistance (some alloys)	

can also be enhanced by the presence of oxygen by promoting the structural stability of the β-phase (Ref 56). Recent theoretical and experimental studies suggest that interstitial oxygen atoms could significantly strengthen the αTi or promote the structural stability of the β-phase (Ref 57). For these types of alloys, the BCC β phases possess good ductility, while the precipitated α phases enhance their strength after aging treatment under defined conditions (Ref 58).

Strong orientation dependence of Young's modulus for a LPBF processed Ti-15Mo-5Zr-3Al alloy was demonstrated by Ba et al. (Ref 59). The Young's modulus of β-phase Ti-alloys strongly depends on the electron–atom ratio, which can be controlled by manipulating the chemical composition and crystallographic orientation. This study is focused on components fabrication from a mixture of pure elemental powders by consolidating them via LPBF. The results of this study showed the formation of a single β-phase without non-molten powders. The texture formation mechanism was also investigated based on the analysis of the solidification of the microstructure. A preferential crystallographic orientation and formation of elongated grains were observed. From the formation of these elongated grains, the epitaxial growth of the previously solidified layer, the cell growth at the solid–liquid interface and the heat transfer and the solidification processes, the mechanisms of formation of texture and texture evolution were also discussed. The kinetic of solidification could not be associated with the change in the crystallographic orientation of the β-phase.

The addition of an insufficient amount of the β-phase SE to some β-phase Ti-alloys or the thermal effects caused by LPBF process induces the transformation of the disordered β-phase to the metastable orthorhombic α″-martensite phase, that is primarily accommodated by internal twinning. This transformation affects the tensile and S_y, making them decrease according to findings from Ref 60.

Traditional βTi-alloys have specific properties. These properties result from the β-phase (BCC) and ω-phase (hexagonal or trigonal). A study of the mechanical properties through cyclic tensile tests and microstructure on β-type Ti-35Nb-2Ta-3Zr alloy fabricated by 3D-Printing was carried out by Chen et al. (Ref 61). Deformational features of specimens were described via TEM observation and crystallographic analysis. The tests allowed to characterize superelastic properties and evaluating the effect of the AM process on the βTi-alloy specimen. This study found an influence of the high oxygen content of the produced specimens on decreasing the superelastic recovery of the alloy. Despite that, the specimens showed efficient tensile properties. Microstructurally, several transformational mechanisms such as twin martensite, zigzag formation, V-shaped formation, stress-induced and twinning-induced ω-structure were evidenced. The βTi-alloys are also considered as alternatives to substitute high strength steels for automotive and energy applications. Components for aerospace applications are always involved in multiple hot workings or thermal treatments to achieve an optimal range of values of strength and toughness.

One characteristic of these alloys is that the β-phase stability, which is a function of its composition, influences the deformation mechanisms during loading. The deformation occurs by conventional viscous slip where the stress induces transformations to include the HCP α′-martensite, the orthorhombic α″-martensite, the HCP ω-phase and twinning. The mechanical response is influenced by the formation of a specific stress-induced mechanism or other mechanisms. These mechanisms depend on the β-phase stability (Ref 62, 63). The mechanism associated with the versatility of β-phase Ti-alloys is related to the fact that their functional and mechanical properties can be custom-made by phase transformations, such as precipitation and martensitic transformation, as described in the followed sections for some of the alloys.

The six metallurgical systems that are the object of study of this review are summarized in Table 2. The subsections presented for each system deal with processing, phase transformation, microstructure and mechanical behavior. The system Ti-Nb is discussed considering different nominal compositions upon adding Zr, Sn and Ta.

4.1 Ti2448 [Ti-24Nb-4Zr-8Sn]

Ti2448 is a near βTi-alloy. The development of this alloy was focused on its use for biomedical applications owing to its low Young's modulus (42-50 GPa)—as compared to other similar titanium alloys (100-120 GPa) and lack of elements with known toxicity for human body (Ref 9, 64-67). It also possesses an improved balance of low modulus and high strength (Ref 68). This alloy can be considered as the most representative of the Ti-Nb metallurgical system. Its general mechanical properties are referred to in Table 3.

This alloy was developed considering the removal of ω-phase by the addition of appropriate alloying elements, depression of martensite start point to below the ambient

Table 2 β-phase Ti-alloys

Metallurgical system/alloy ID	Nominal composition, wt.%	MoE, %	Classification	Application sector
Ti2448	Ti-24Nb-4Zr-8Sn	6.7	Near β	BIO
Ti1023	Ti-10V-2Fe-3Al	9.6	Near β/Metastable β	AER
Ti5553	Ti-5Al-5V-5Mo-3Cr-0.5Fe	9.5	Near β	AER
Beta C	Ti-3Al-8V-6Cr-4Mo-4Zr	16.0	Metastable β	AER
Alloy C	Ti-35V-15Cr	47.5	Stable β	AER
System Ti-Nb	Ti-13Nb-13Zr	3.6	Near β	
	Ti-35Nb-7Zr-5Ta	10.9	Metastable β	
	Ti-33Nb-4Sn	9.2	Near β	BIO
	Ti-35Zr-28Nb	7.8	Near β	

temperature so that the transformation can be stress-induced, complete control of the intrinsic elastic modulus of β phase and, finally, no affectation of strength as a result of alloying. The action of Zr and Sn is focused on suppressing the α″-martensitic transformation. By first-principles calculations (i.e., a method to calculate physical properties directly from basic physical quantities) (Ref 69), it was estimated that the addition of Nb to Ti increases significantly both the elastic and phase stability of the β-phase. In addition, the presence of both Zr and Sn makes this alloy completely stable and functional in terms of low elastic modulus and stability of the phase.

Because Ti-Nb is a β-isomorphous system, it is necessary to keep the Nb content to a minimum to minimize the elastic modulus. In this way, this alloy is of great interest for biomedical applications. A significant difference between human bone's elastic modulus and biomedical implant's elastic modulus produces stress shielding after the implant is placed (Ref 66, 68). One common method to reduce the modulus of a material is to introduce porosity into the structure. In bone tissue engineering applications, porous materials are important due to their low modulus, coupled with the possibility of enhancing the biological fixation through bone cell in-growth (Ref 67).

Besides low elastic modulus and high strength, it is also required high yield strength and fatigue resistance for this alloy to be adequate on implant applications. Ti2448 has been found to experience superelasticity that involves new mechanisms of significant lattice distortion and homogeneous nucleation of dislocation loops. Stress-induced martensitic transformation is also present in addition to superelasticity phenomena (Ref 68, 69).

4.1.1 Processability via LPBF. During processing of Ti2448 via LPBF, a tendency of density increase when scanning speed is around 600 mm/s has been reported by Liu et al. (Ref 68). Beyond this value of scanning speed, the density tends to a plateau at values higher than 99%. A high incident energy density results in a large amount of melting and, consequently, a higher final density. A similar tendency was reported by Froes and Qian and Yang et al. (Ref 67, 70) at comparable processing parameters and conditions.

According to Ref 67, at laser scanning speeds between 500 and 750 mm/s, the amount of the volume of porosity decreases. The average pore size was characterized as a sphere that has the same volume as the measured pore. At large pore sizes (> 50 μm), the pore distribution was not uniform, except for scanning speed 500 mm/s. At this scanning speed, an increase in the pore distribution homogeneity was observed. The amount

Table 3 Ti2448 general properties

Density, gr/cc	$T_β$, °C	UTS, MPa	S_y, MPa	ε, %	E, GPa
5.34	…	830-910	790-900	7-9	42-50

of large pores affects both the average pore size and the relative density.

The presence of porosity was studied in Ref 60, 70 with two similar compositions focused on fully dense structures and porous structures. Although compositions were not the same, the opposite happens with the constituents. Differences lied on stoichiometry mainly. On the one hand, the recoil pressure observed in the results of Ref 60, caused by metal vaporization, provides to liquid the ease of being away from the melt area, thereby promoting the porous generation. Since Sn has the lowest boiling point—around 2690 °C—among the alloy components, it vaporizes in preference to other constituents. The porous presence affected the mass density and alloy composition. Besides these two affected features, columnar structure and grain size led to different mechanical properties. The high energy density was also detected to play an important influence on the decreasing of strength, ductility and porosity increasing. At the same time, low energy density was detected to promote the presence of unmelted Nb particles which negatively affected the ductility facilitating the propagation of cracks.

On the other hand, the performance of porous structures of Ti2448 processed via LPBF was investigated in Ref 70 under the presence of porosity. As for preferential crack initiation sites where porous are present, the number of cycles to failure at those zones was correlated to the size of the pores. Below the critical value of fracture toughness, fatigue cracks may initiate at the porosity zones but do not propagate until failure. According to the results of this study, the stress intensity around pores did not reach the critical value of fracture toughness. The size of the optimal molten pool was about 146 ± 17 μm. The process parameters to reach such molten pool size were defined as follows: power of 150 W, scanning speed of 750 mm/s, laser spot size of 40 μm and hatch spacing of 100 μm.

High scanning speeds produce balling and dross formation in the molten pool and in its vicinity because of instabilities in the molten pool, according to Ref 14. Those high enough scanning speeds lead to poor surface finishes but near fully

density when Ti2448 is processed via LPBF. For speeds higher than 300 mm/s, the experimental results showed a strong correlation between Vickers hardness and density. At lower speeds than 300 mm/s, the hardness remains high, despite the decrease of the density. Based on this study, to successfully manufacture near full density parts of Ti2448 with an acceptable surface finish, an optimum laser scanning speed must lie between 300 and 600 mm/s. However, since the speed and the processing cost of manufacturing via LPBF are directly related to the scanning speed, there is a considerable benefit upon using values near to the upper limit of the range.

Based on literature and features about material response and mechanical behavior of this composition, a process parameters window for processing this composition via LPBF can be considered from the ranges of parameters in Table 4.

4.1.2 Phase Transformation and Microstructure. The potential phase transformation and β-phase stability can be improved by interstitial oxygen in the β-phase. In compositions where the oxygen content is high enough, the amount of nonlinear recoverable strain is reduced, and the double yielding phenomenon can also be covered. At oxygen levels between 0.08 and 0.40 wt.%, the nonlinear recoverable strain of Ti2448 decreases from 1.2% to near 0% (Ref 68). During the LPBF process, the oxygen enrichment is small (about 0.04 wt.%), which means that the use of low oxygen content powder may produce a recovery of pronounced superelastic behavior.

The electron/atom ratio determines the stability of the β phase of this alloy. Despite this, Young's modulus increases with the solute content. As shown in Fig. 5 (Ref 73), at a low electron/atom ratio with decreasing solute concentration, the β-phase becomes less stable and the formation of the α-phase or α'-martensite causes the elastic modulus to increase. The peak in the middle (red circle) is caused because of the formation of metastable ω-phase, which has a higher elastic modulus than the β-phase. The effect of the α''-martensite is superimposed on the curve and its formation helps to shape the valley left of the peak.

The constituent phases of this alloy are based on β-phase mainly, but it could be accompanied by metastable phases ω and α''. However, there exists a composition range in which the β-phase is sufficiently stabilized to be alone. This composition range corresponds to the dotted curve of Fig. 6.

An effective way to decrease the elastic modulus of this alloy is by promoting the formation of a microstructure with a monolithic β phase. A two-phase microstructure with acicular α precipitation distributed along the grain boundaries of the β matrix was observed in sintered samples (Ref 74). It was also observed that the sintered density increased with increasing temperature and the measured relative density in samples was around 97.6%. The microstructure with monolithic β-phase was achieved by solution treatment at 1000 °C and subsequent
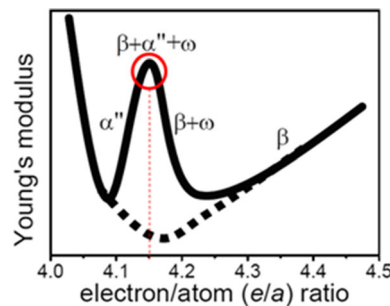

Fig. 5. Variation of the Young's modulus with the electron/atom ratio in Ti2448. Reprinted from Ref 73, Copyright 2007, with permission from Elsevier

water quenching. This post-thermal treatment also suppressed the formation of α-phase.

By spark plasma sintering (which is a novel sintering technique that uses pressure-driven powder consolidation in which a pulsed direct electric current passes through a sample compressed in a graphite matrix), samples of Ti2448 were produced. A metastable β phase, a primary α phase and α''-martensite were identified after a solution treatment at 850 °C (Ref 75). Variation in aging times showed an increment in the content and grain size of the secondary α phase, which was observed to be precipitated directionally from the β-matrix. Compressive strength and elastic modulus were observed to increase after a solution and aging heat treatment. On the other hand, the ductility increased at first but decreased at the end. The presence of such heterogeneity of phases as a result of solution and aging heat treatment showed a relative non-homogeneous mechanical response of the alloy.

4.1.3 Properties. Zr acts as a very efficient strengthener in this alloy whose tensile strength after hot work ranges between 700 and 930 MPa depending on the interstitial content. However, the processing conditions of the alloy will determine the final mechanical properties, as well as its performance. Regular values of Young's modulus, S_y and UTS of this alloy processed by LF are about 53 GPa, 570 and 670 MPa, respectively (Ref 68). Moreover, some pronounced superelastic deformation behaviors were observed in some samples of this study. Such behaviors were reported influencing the general tensile properties.

Taking advantage of the versatility of LPBF for manufacturing lattices and scaffold structures, a simultaneous improvement in strength and plasticity has been achieved by Liu et al. (Ref 71). This improvement is related to the unique structure formed during LPBF process, i.e., "hard-wraps-soft" structure of the microscale molten pools. Fine and hard grains distributed

Table 4 LPBF process parameters for processing Ti2448.

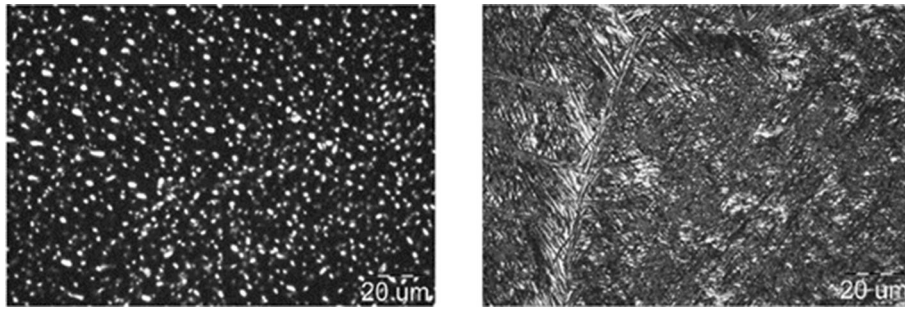| Refs.	Preheating, °C	Power, W	Laser spot, µm	Layer thickness, µm	Hatch spacing, µm	Scanning speed, mm/seg
Ref 68	Not rep.	200	80	100	Not rep.	550-800
Ref 67	Not rep.	175	40	50	100	500-1500
Ref 70	200	175	40	50	100	750
Ref 71	200	200	Not rep.	50	100	1000
Ref 72	Not rep.	200	40	50	100	750

Fig. 6. Left: light optical in the STA condition showing globular primary α (light) and dark etching aged beta matrix. Right: light optical in the BASCA condition showing coarse α platelets and minor amounts of retained β (light). Reprinted by permission from Springer Nature Customer Service Centre GmbH: Springer Nature, *JOM,* State of the Art in Beta Titanium Alloys for Airframe Applications, James D. Cotton et al. (Ref 35), Copyright 2015

along the edge of the molten pool were observed and associated with the high strength in the samples fabricated with Ti2448.

Scaffold structures processed by LPBF were analyzed under compression tests and variation of laser scan speed and constant laser power (Ref 67). Rotation between layers was considered part of the scanning strategy to homogenize heat distribution and control the evolution of microstructure. Some porosity was detected and associated with the evaporation of Sn. This porosity is related to the relatively low density in some samples and was found to occur at lower scan speeds. Compression tests showed excellent mechanical performance on samples produced at 750 mm/s scanning speed with low solid section density.

4.2 Ti1023 [Ti-10V-2Fe-3Al]

It is classified as a near βTi-alloy (Ref 76-78) and metastable β Ti-alloy (Ref 50, 57, 79-84). An improved combination of good strength, deep hardenability, fracture toughness and good ductility were the main properties taken as objective to look for by developing this composition. This composition was developed as a forging alloy for applications in the aerospace industry. This alloy became the most visible and important in the aerospace industry (airframes, landing gear components, etc.) for applications up to 315 °C after regular applications in the same industry were performed with Ti-13V-11Cr-3Al (Ref 35, 85). Its general mechanical properties are referred to in Table 5. Hot die and conventional forgings are also some sporadic applications of Ti1023. Structurally, this alloy offers weight savings by using it instead of components made of maraging steels.

In this alloy, the BCC β-phase is stabilized by Fe and V additions. Al acts as a solid solution strengthener for the low-temperature precipitating α-phase. Regardless of whether the microstructure is composed by homogeneous β or a mixed (α + β) microstructure, the stability of the β-phase can be manipulated in such a way that a martensitic transformation takes place when enough compressive or tensile stresses are applied. The bimodal microstructure consisting of α grains in β-phase globular matrix gives birth to a superior combination of strength and ductility (Ref 78). As a result of the good properties that are a consequence of the deep hardenability, this alloy can develop a wide variety of strength levels depending on the selection of heat treatment (Ref 76, 84). A relative tendency of microsegregation in the form of β fleck defects is known by producers of ingots of this composition (Ref 35). There have been developed practices of melt and thermal

Table 5   Ti1023 general properties

Density, gr/cc	T_β, °C	UTS, MPa	S_y, MPa	ε, %	E, GPa
4.56	790-805	965-1240	1150-1170	9-11	106-110

treatment to minimize the potential of the evolution of that microsegregation. This issue is more related to property variability than for mechanical responses associated with fatigue cracks evolution.

In general, Ti1023 may undergo deformation via deformation of stress-induced martensite. The control of this mechanism provides a new route to optimizing the load-bearing capabilities of the alloy. The stress-induced martensite formation starting from the metastable β-phase can lead to an improved balance of strength and ductility (Ref 77).

4.2.1 Processability via LPBF. Relatively scarce information is available about investigations of Ti1023 processed via LPBF. Two recent research works (Ref 86, 87) evaluated samples of this composition under different processing conditions via LPBF. The first work used a range of characterization techniques and properties to evaluate material performance through tensile testing. The development of fine β columnar grains and widespread cell structures was observed upon printing with a small powder layer thickness, a low laser power and a short exposure time. These process conditions configure the scenario for a low energy density. By setting a high value of laser power and exposure time (high energy density), an increase in grain growth and texture was observed together with a decrease in cell structures. Also, athermal ω (ω_{ath}) precipitates were observed in all printed samples. ω_{ath} is often observed in β-phase Ti-alloys and affecting the elastic modulus and strength. Some samples showed to have a hybrid grain structure. This microstructure has a highly limited ductility because of intergranular fracture. The fine columnar grain obtained was beneficial to both ductility and strength, while the hybrid grain structure reported on some samples also promoted weakened grain boundaries. It was observed as non-uniform grain morphologies and inhomogeneous grain size distribution.

The second work studied samples fabricated horizontally and vertically with two different energy densities. The as-fabricated horizontally printed samples with lower energy density showed β and athermal ω phases, while the vertically

printed samples showed the same two phases and nanosized α laths. Anisotropic behavior of plasticity was observed in the samples made with the lower energy density. The presence of both phases in the first work was confirmed in the second work. The different energy values allowed the development of those two phases adding nanosized α laths on vertically built samples. The presence of α-phase established the difference in ductility while maintained S_y and UTS.

A different stoichiometrically composition with the same constituent elements processed via LPBF was studied in Ref 88. The alloy composition used was Ti-1Al-8V-5Fe. Elemental powder of Ti and Fe, and an Al-V master alloy powder with irregular shape were used to produce the components through LPBF. Ultra-high strength and relatively good ductility values were achieved as a result of a very fine grain microstructure with nanoscale precipitates after microstructure analysis. Fe segregation was detected without detrimental consequences on the mechanical behavior of the alloy.

Although this alloy does not have the same composition as Ti1023, LPBF process parameters like laser power 370 W, scanning speed 1035 mm/s, hatch spacing 0.12 mm and layer thickness 60 μm, could be considered a good starting point for defining the optimal window parameters. The base plate was preheating at 80 °C and a stripe laser pattern was set up in the system for the sample printing. On the current layer, the stripes were rotated counterclockwise by 67° with respect to the previously deposited layer.

The LPBF processed material showed a very high compression strength, reaching values around 1.7 GPa when the plastic strain before the failure point was 0.1. The hardness measured value was around 470 HV. Thermal-treated samples produced an increase in compressive strength and strain to failure reaching 1.8 GPa and 0.3, respectively.

Based on literature and features about material response and mechanical behavior of this composition, a process parameters window for processing this composition via LPBF can be considered from the ranges of parameters in Table 6.

4.2.2 Phase Transformation and Microstructure. Phase transformations such as $\beta \rightarrow \alpha''$ martensitic transformation, athermal or isothermal $\beta \rightarrow \omega$ and $\beta \rightarrow \alpha$ transformation can be present in Ti1023. As mentioned in the previous section, the phase transformation $\beta \rightarrow \alpha''$ could be induced by stress, including internal stresses arising from quenching and external stresses such as tensile loading or mechanical polishing (Ref 57). By heating the alloy to a temperature above T_β followed by cooling below the temperature of β-phase stability, the α-phase brings the appearance in the form of needles and its amount depends on temperature and time of annealing. The control of temperature and time of thermal treatments enables the evolution of the α-phase morphology and it also allows to obtain the required properties in a wider range of possibilities (Ref 79, 89).

The sequence of the phase transformation upon quenching evolves with the heating rate by analyzing the continuous evolution of crystallographic relationships between phases. At low temperature values, the reverse transformation of α″ into β occurs. This reversion happens to a larger extent considering an increasing heating rate (Ref 50). Under quenching conditions, the stable α-phase can be generated from three different sources: the ω-phase, the α″-martensite and the β-phase.

In the case of thermal treatments of Ti1023 performed in atmospheric environments, the influence of oxygen in the system is inevitable. This influence in microstructural evolutions in the processes of hot working or thermal treatments has not been studied deeply (Ref 57).

4.2.3 Properties. The mechanical properties of this alloy depend strongly on the structural stability and phase transformations, such as martensitic transformation and precipitation (Ref 57, 83). Volume fraction, grain orientation, grain size and phase morphology of β-phase, α′ and α″ phases have also been largely associated as strong features that influence the mechanical properties in Ti1023. Based on Ref 81, these factors also affect the deformation behavior in different deformation patterns. Microindentation and nanoindentation tests with higher sensitivity and precision, micromechanical behavior of microphase or nanophase can be obtained.

Similar alloys as Ti1023 with low stacking fault energies are prone to experience discontinuous recrystallization upon defining or knowing the preferable flow localization, which produces inhomogeneity of grains (Ref 78).

According to Ref 79, the α-phase content does not significantly influence on the mechanical properties of Ti1023 after heat treatment. Results reported an increase in the yield point due to the rise amount of the β-phase of higher strength. Correspondingly, a decrease of impact strain was detected because of a decrease in the amount of the α-phase. The morphology evolution of phases was also observed and associated with the behavior of yield point and impact strain.

Different deformation mechanisms of Ti1023 were studied from the effect of microstructures on them (Ref 80). In (α + β)-phase field solution treatment conditions, the fraction of globular α-phase was observed to decrease, while the compression strength increased. Under conditions of heating time increasing, the fraction of the acicular α-phase increased as well as the compression strength. Under aging conditions, the microstructure and mechanical properties did not change with the aging time as expected concerning similar previous results.

The indentation deformation behavior of β-phase in Ti1023 was investigated in Ref 81. The alloy was modified by the β solution treatment that involved water quenching. The treatment temperature, loading rate and indenter load were taken as objective parameters to analyze their influence on micromechanics properties. Decreasing behaviors in the microhardness and Young's modulus were detected until a certain load was assessed. Both properties were observed to remain at the same level when the indenter load was above such critical value. On the other hand, the dissipation of the plastic energy was observed to be significantly influenced by the β solution

Table 6 LPBF process parameters for processing Ti-1023

Refs.	Preheating, °C	Power, W	Laser spot, μm	Layer thickness, μm	Hatch spacing, μm	Scanning speed, mm/seg
Ref 88	80	370	Not rep.	60	120	1035
Ref 86	Not rep.	200-400	Not rep.	30-60	60-75	5000
Ref 87	Not rep.	200-400	70	30	60	750-1200

treatment temperature and loading rate. The load value was also observed to influence the plastic energy dissipation, which increased with the growth of the indenter load exerted on the specimens.

4.3 Ti5553 [Ti-5Al-5V-5Mo-3Cr])

It is a near βTi-alloy. This composition was developed to provide processability, a lesser propensity to segregation, a lower cost and a better performance—among others—over the already established composition Ti1023 used in similar applications (Ref 85). Its general mechanical properties are referred to in Table 7. In aeronautical applications, it is widely used in landing gear modulus, helicopter rotors, wings and load-bearing fuselage components on civil (B787 Dreamliner, Airbus A350) and military aircrafts (Airbus A400M). This alloy is characterized by the versatility of its mechanical properties (high strength, highly hardenable, ductility, low density) based on the post-processing thermal treatment, which makes it attractive as a structural titanium alloy (Ref 35, 90, 91).

Due to α precipitates formed during aging, the strength is significantly higher, and the processing temperature of this alloy is lower than that of dual $(\alpha + \beta)$ phase alloys. High ductility and high strength are reached by the application of heat treatments (Ref 92). Commonly, the production of parts manufactured with this alloy includes a complex sequence of different thermomechanical steps until obtaining the desired microstructure. Large-sized components are commonly manufactured by the forging process (Ref 93).

A slightly different composition than Ti5553 that is recently being study is Ti55511 (Ti-5Al-5V-5Mo-1Cr-1Fe). It is also a near β Ti-alloy with an application niche in the aeronautical industry (Ref 94). Compared to Ti64 (Ref 95), Ti55511 has superior structural properties as it provides higher strength with 15-20% less weight. As compared to Ti5553, the addition of Fe and reduction in Cr makes the alloy less prone to segregation. It allows ingots to be produced at a higher amperage and melt rates, which result in a significant reduction in the process cycle time.

4.3.1 Processability via LPBF. Comparatively, this alloy indicates a larger processing window and a higher working strength than Ti1023. Furthermore, Ti5553 is characterized by a demonstrated weldability (Ref 93).

The energy density must be carefully tuned to have the optimal grain size distribution to achieve high material density. During the mechanical behavior analysis of Ti5553 performed by Schwab et al. (Ref 93), a UTS of about 800 MPa and a strain up to 14% were obtained by evaluating cubic samples processed with different scanning strategies. The processability of this material was confirmed based on relatively good values obtained from different processing conditions. Results from UTS and strain were added to the obtained density near 99.95%.

Ti55511 was investigated by Schwab et al. (Ref 94) through processing and manufacturing blocks via LPBF recently. As mentioned in Sect. 4.2, this composition slightly differs from Ti5553 by having less Cr content and adding Fe, which diminishing the possibility of segregation and favoring the production process of ingots (Ref 94).

As to LPBF process of Ti55511, results from the mentioned study showed that the process optimal parameters for obtaining density values higher than 99% are as follows: power at 200 W,

Table 7   Ti5553 general properties

Density, gr/cc	T_β, °C	UTS, MPa	S_y, MPa	ε, %	E, GPa
4.58	820-880	1175-1300	1000-1100	6-8	…

scanning speed of 300 mm/s, hatch spacing of about 0.21 mm and layer thickness of 50 μm. Preheating was also tuned for diminishing the probability of segregation and reducing the residual stresses. Microhardness values obtained were around 320 HV with small statistical deviation on data. The relatively small variation was related to a uniform microstructure, as stated in section 5.2.1. Relatively high surface quality was also obtained. Although this feature is not inherent to the alloy composition itself, it is worth mentioning that the identified optimal process parameters can provide such good condition. The dominant β phase in the original powder was not almost transformed after processing. It could have been expected to happen as occur with some Ti-alloys.

Based on literature and features about material response and mechanical behavior of this composition, a process parameters window for processing this composition via LPBF can be considered from the ranges of parameters in Table 8.

4.3.2 Phase Transformation and Microstructure. The microstructure of this alloy consists of HCP α-phase ($P6_3/mmc$) embedded in the BCC β-phase ($Im/3m$) (Ref 92). When processing via LPBF, precipitation of the α-phase can occur in the vicinity of the heat-affected zone (HAZ), which typically reaches temperatures close to T_β. The dissolution of preexisting base metal α-phase precipitates can occur near HAZ when T_β is exceeded. The extent of these phase transformations depends on the cooling rates and thermal history of the part being processed (Ref 96). These two factors are inherent to process conditions.

In the microstructural analysis performed in Ref 92 on cubic samples with densities near to 99% under preheating conditions, there were no indications of a third phase. Due to the presence of a high amount of β-phase SE, the possibility of the existence of martensitic α′-phase is low. β-phase SE suppresses the martensite formation. The micrographs showed typically elongated grains growing across the layers, while cellular solidification or segregation, in general, was not obtained like in other Ti-alloys. The microstructures of all samples were composed of large β grains elongated in the building direction and dispersed α-phase precipitates. The α-phase morphology was detected in the shape of small plates sizing around 1 μm. The mechanical properties of samples were enhanced by the presence of α-phase, which strengthens the β matrix acting as a reinforcement. Based on this study, it could be demonstrated that the phase formation during the process can be influenced by substrate heating.

The heat treatability of Ti5553 processed via LPBD was analyzed through the investigation of Ref 96. As in Ref 92 where the presence of a large amount of β-phase SE influenced martensitic α′-phase, the microstructure of this study retained β-phase upon high cooling rates inherent to LPBF by the presence of such stabilizers. This microstructure allows the possibility for post-build heat treating to enhance or modify the properties of Ti5553 upon LPBF processed. It can be possible, differently than other Ti-alloys, to produce a range of microstructures with

Table 8 LPBF process parameters for processing Ti5553

Refs.	Preheating, °C	Power, W	Laser spot, μm	Layer thickness, μm	Hatch spacing, μm	Scanning speed, mm/seg
Ref 92, 93	Not rep.	60-140	80	45	Not rep.	100-180
Ref 90	200	400	80	30	80-120	Not rep.
Ref 96	Not rep.	100	50	30	Not rep.	600
Ref 94	250	200	Not rep.	50	210	330

different morphologies and ratios of both α and β phases. Different heat treatment groups were defined during the experimentation campaign. For all these groups, the SEM analysis revealed a primarily equiaxed β-grain microstructure. All groups had densities around 0.8% less than full density value (4.65 g/cm^3). A significant amount of α-phase in the microstructures at high temperatures was present. However, high strength and high ductility in the α/β microstructure resulted in subjected of morphology and volume fractions of phases. Under low temperatures for aging, ω-phase could be present, which significantly affects subsequent secondary α distributions and the balance between strength and ductility. Typical microstructures of Ti5553 processed via STA and BASCA are shown in Fig. 6 (Ref 35).

4.3.3 Properties. High ductility with low as-built hardness is typical on Ti5553 as compared to Ti64. It helps minimize distortion, residual stresses and cracking when producing thick parts via LPBF (Ref 90, 96). This alloy composition can strengthen via both solid solution mechanisms in the single phase and precipitation strengthening of α-phase at temperatures below the T_β around 850 °C (Ref 97). Material densities of about 99.93% can be achieved by selecting an optimized value of energy density. However, it finally depends on the geometry of the component to be printed and the inherent features of powdered material like the atomization process, particle size distribution, morphology and initial porosity if it applies.

Experimental data show that the oxygen content of this alloy is relatively low as compared to many Ti-alloys. It enhances its ductility and toughness of the system. On the other hand, increasing the cooling rate from the solution temperature and lowering the aging temperature relative to a baseline heat treatment (either STA or BASCA) would provide high strengths while ductility is maintained at adequate values. The castability of this composition was evaluated in Ref 98. Among the obtained findings, it was confirmed that under the mentioned process conditions, the UTS could be reach values near to 1100 MPS, σ_y near to 1035 MPa and elongation in the range of 6.0-8.0%. To the extent that more precise thermal treatment parameters can be tuned to work with, *Widmanstätten* structures can be given to birth, which becomes a key factor for obtaining superior tensile strength properties in this alloy.

Bulk parts with improved mechanical properties by precipitation hardening may be manufactured with this alloy by processing via LPBF when additional substrate heating during the printing process is applied. Besides, thermal distribution in this scenario must be considered for taking advantages of distortion control and residual stresses minimization.

Microhardness and mechanical behavior under compression of cubic samples processed via LPBF and subjected to thermal conditions were evaluated by Zhao et al. (Ref 92). The existence of α-phase precipitates was associated with the

Table 9 Beta C general properties

Density, gr/cc	T_β, °C	UTS, MPa	S_y, MPa	ε, %	E, GPa
4.77	715-740	1276-1413	1160-1180	6-8	103-107

enhancement of microhardness on about 60% on two different thermal conditions. The influence of residual stresses inherent to LPBF on the microhardness was just mentioned as possible to happen but not formally concluded.

This alloy generally shows that β-phase is more ductile than α-phase due to its higher number of slip systems. In this study, the microhardness measurements and the compression tests showed the same behavior for the two thermal conditions.

At $\sigma > 700$ MPa and $\varepsilon > 0.02$, stress-induced $\beta \rightarrow \alpha''$ transformation was observed during uniaxial compression performed on cubic samples obtained directly from as-fabricated ingot of Ti5553 and quenched from the β field (Ref 99). In this work, deformation mechanisms of this alloy were determined. At the specified mechanical condition, the yield stress of the alloy has already been reached. This specific transformation is not commonly observed in βTi-alloys. Some internal strain distributions were observed within α'' colonies, indicating that plastic deformation can be related to the existence of this phase (Table 9).

4.4 Beta C [Ti-3Al-8V-6Cr-4Mo-4Zr]

It is a metastable βTi-alloy (Ref 35, 44, 100, 101). Its development was also for substituting Ti-13V-11Cr-3Al for aerospace applications as well as focused on the manufacturing of springs and fasteners. Cold and hot workability, optimum density, easy ingot manufacturing and mechanical properties were highly considering for the alloy formulation. Metastable βTi-alloys do not develop as high a strength as the near βTi-alloys (Ti2448, Ti5553).

This alloy also features because of being easy to melt and less prone to segregation due to the low Cr content by adjusting the amount of other β-phase SE. It can also be hardened by the solution plus aging treatment (STA) reaching UTS values near to 1400 MPa (Ref 58, 97). It is one of the Ti-alloys that can be solution-treated at T_β. Typically, the range of temperature for solution treatment is between 790 and 925 °C, time between 0.5 and 1.0 h, followed by either water quenching, air cooling or forced air cooling depending on the section size (Ref 9, 58).

In the STA condition, this alloy can contain HCP α, BCC β (solute rich), β′ (solute-lean β), ω, TiCr$_2$ and (Ti, Zr)$_5$Si$_3$ particles. Both the ω phase and TiCr$_2$ are embrittling (Ref 64).

The presence of secondary phases such as ω and $TiCr_2$ is detrimental for the mechanical performance of components.

The application of this alloy was expanded to the oil and gas industries after certification of the composition on superior corrosion resistance in reducing acids and hot chloride environments. When very high strength, low modulus, light-weight and corrosion resistance are key factors for satisfying the functional and application requirements, the Beta C alloy is adequate.

As it happens with other βTi-alloys, there are restrictions for Beta C to be continuously used because of the limited recycled material availability, which results in high alloy cost, special care requirements upon melting and processing (Ref 35).

4.4.1 Processability via LPBF. Information about the processability of Beta C via LPBF is scarce by now. A few related works appear reported in the literature (Ref 102-104). The second and third works are based on WAAM (this process is based on the combination of an electric arc as a heat source and wire as feedstock) (wire + arc additive manufacturing) process. In Ref 102, cubic samples of Beta C and Ti64 were processed with the same process parameters: power 1.3 kW and laser scanning speed 4000 mm/s. The values of density reached were around 98%. The particle size for Beta C was in the range between 20 and 80 μm. Tensile tests were performed according to ASTM E8/E8M standard with "dog-bone" specimens machined from LPBF processed samples.

The work reported in Ref 103 was focused on analyzing the grain refinement and the columnar to the equiaxed transition of some Ti-alloys. On the one hand, the mechanical and microstructural responses to thermal treatments after WAAM processing were evaluated in Ref 104.

The WAAM process differs from LPBF process on features like delivered power upon melting and the yield of the process. The two works based on WAAM are mentioned since this process belongs to additive manufacturing processes. However, the metallurgy of materials processed through WAAM as well as the mechanical behavior after testing and analysis cannot be compared either taken as a reference because of the nature itself of the two processes. These two works evaluated Beta C compared with referencing alloys. Based on the microstructural analysis from Ref 102, Beta C shows good potential for making large volume parts in high power and high scanning speed processed via LPBF.

Based on literature and features about material response and mechanical behavior of this composition, a process parameters window for processing this composition via LPBF can be considered from the ranges of parameters shown in Table 10.

4.4.2 Phase Transformation and Microstructure. The typical aging cycle of Beta C is 470-620 °C for 4-12 h based on the final geometry of the component and the desired mechanical properties. As stated in the previous section, several phases are possible to be formed due to the complexity of the chemistry and ability to form metastable phases (Ref 35, 49).

The enriched β phase has been suggested to decompose by a phase separation reaction into solute-rich and solute-lean β: $\beta_{SS} \rightarrow \beta + \beta'$ and by more complex reactions.

In the solution annealed condition, Beta C shows a microstructure that consists of a metastable β phase, which is readily retained at common section sizes by air cooling or water quenching. Based on the thermomechanical processing history and the section size, the β grain size varies. In the STA condition, increases in the strength in the order of 40% can be obtained by precipitation strengthening.

The phase separation reaction $\beta_{SS} \rightarrow \beta + \beta'$ was reported to be unexpectedly observed upon short times aging at 350 and 550 °C by Barriobero-Vila et al. (Ref 100). This final observation was supported by the fact that ω-phase had been reported to occur at 310 °C in this alloy. Consequently, with this microstructural behavior, the β' precipitate formation was observed to produce little or no increase in strength.

The effect of addition of Si (around 0.05%) on this composition in terms of the microstructure was studied by Qi et al. (Ref 58). The presence of Si produced finer grain size in the composition which stated a difference in tensile properties. According to the *Hall–Petch* relationship, the grain refinement enhances S_y and the formation of fine silicides dispersed in the system affects precipitation strengthening. These two facts explained the difference in the tensile properties, as was mentioned above.

Upon LPBF processing this alloy, a fully β microstructure with grains elongated in the building direction was obtained according to results from Ref 102. The presence of this microstructure resulted in low strength, but relatively high ductility and fracture toughness as compared to Ti64 also processed via LPBF.

4.4.3 Properties. Through a precipitation strengthening mechanism, increases in strength in the order of 40% can be possible to obtain as mentioned in the previous section. This alloy can be stress relieved in the range of 705-760 °C for 10-60 min. On the other hand, cold work increases the strength of the alloy in the solution-treated condition and accelerates the aging response. Depending on the product geometry, orientation and final strength level after STA, the fracture toughness value can be reached in the range of 49-88 MPa $\sqrt{m}$ (Ref 35, 85).

Water quenching before aging at different temperatures was performed on hot-rolled samples in Ref 100. Specifically, a brittle behavior at 350 °C after an exposure time enough to give birth to α-phase was observed in this alloy. The formation of shallow dimples because of microvoid coalescence promoted the failure in ductile samples. Many cracks were also observed. The best combination of ductility and strength was observed with large type 2α precipitates formed in the β matrix upon aging above 500 °C. These precipitates do not obey the Burgers OR of the system (shown in Sect. 3). On the other hand, fatigue crack propagation was also observed to be faster in this alloy

Table 10 LPBF process parameters for processing beta C

Refs.	Preheating, °C	Power, W	Laser spot, μm	Layer thickness, μm	Hatch spacing, μm	Scanning speed, mm/seg
Ref 102	Not rep.	1300	Not rep.	50	Not rep.	4000

compared to Ti64 with the main effect of Beta C microstructure prone to change the fracture surface morphology.

Variations on this composition by adding Si also showed improvements in creep resistance and inhibition of β grain growth of the alloy. However, the addition of high amounts of Si negatively affects the ductility of Ti-alloys at room temperature (Ref 35).

4.5 Alloy C

It is a stable βTi-alloy. This alloy was developed to be a non-combustible material for aeronautical applications. A ternary system Ti-V-Cr like this satisfies the non-susceptibility to sustained combustion and resistance to excessive temperatures and stresses. This alloy also provides a significant weight-save as compared to nickel-based superalloys (Ref 35, 105), when fabricating components of reaction engines. Its general mechanical properties are referred to in Table 11. This alloy is essentially a stable β-type Ti-alloy. It implies that quenching is not required to retain the predominant β phase. Significant α precipitation neither occurs upon aging (Ref 9, 64). The presence of Cr improves the oxidation resistance and depresses the melting point, which in turn assists in retarding sustained combustion by absorbing energy to the heat of fusion. The effect of Cr on the burnability of this alloy is shown in Table 12 (Ref 106).

The content of V does not significantly affect the burning resistance behavior. Other alloying elements will change the position of the α/β phase boundary, the melting point through and the exact amount of Cr necessary for nonflammability.

4.5.1 Processability via LPBF. Related works of Alloy C processed via LPBF are not reported in the literature. The potential applications of this alloy composition as non-burning material make it very attractive for aeronautical and aerospace applications where components are subjected to high-temperature regimes or could be exposed to conditions in which self-ignition could happen.

4.5.2 Phase Transformation and Microstructure. The evolution of the microstructure of this alloy has not been studied deeply. The microstructure after cast processing basically consists of recrystallized equiaxed β-phase, some small volume fractions of titanium carbides and α-phase. Based on the equilibrium of ternary systems, titanium carbides are expected to precipitate within the α phase (Ref 35). A micrograph showing the microstructure of this alloy is shown in Fig. 7.

A reference work (Ref 107) reported a microstructure of this alloy based on titanium carbides in a βTi matrix, as shown in Fig. 8. The average grain size reported is in the range of 3-5 mm by checking on a macroscopic section of the ingot of material which was produced by three-time vacuum arc remelting (VAR):

It is also observed that the β matrix seems stable in domains far from those particles. The addition of C in this composition also showed an increase in creep resistance. This was attributed

Table 11 Alloy C general properties

Density, gr/cc	T_β, °C	UTS, MPa	S_y, MPa	ε, %	E, GPa
5.28	N/A	930-1025	865-980	21-24	…

Table 12 Burn test results of Ti-V-Cr ternary system (Ref 106)

| Ti-alloy	V	Cr	Other	Result
Bal.	13	11	3Al	Burns
Bal.	35	15	…	Non-burning
Bal.	25	15	…	Non-burning
Bal.	30	15	…	Non-burning
Bal.	25	35	…	Non-burning
Bal.	35	15	0.5 Hf	Non-burning
Bal.	35	15	2 Si	Non-burning
Bal.	30	15	5 Nb	Non-burning
Bal.	35	15	4 Zr	Non-burning
Bal.	35	15	2 Mo	Non-burning
Bal.	35	15	3 Fe	Non-burning
Bal.	35	15	2 Co	Non-burning
Bal.	35	15	4 Co	Non-burning
Bal.	35	15	6 Co	Non-burning
Bal.	35	15	1 Ru	Non-burning
Bal.	35	15	3 Ru	Non-burning
Commercial Alloys Ti64, Ti6242				All burn
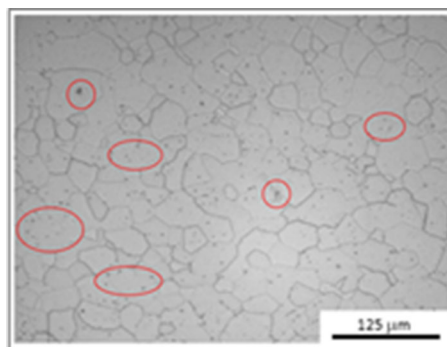
Fig. 7. Micrograph showing the microstructure in which dark zones may be α phase or carbides. Reprinted by permission from Springer Nature Customer Service Centre GmbH: Springer Nature, *JOM,* State of the Art in Beta Titanium Alloys for Airframe Applications, James D. Cotton et al. (Ref 35), Copyright 2015
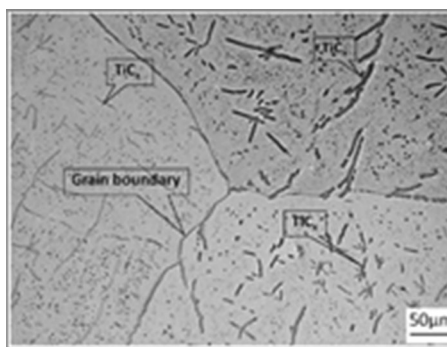

Fig. 8. Micrograph taking from a triple grain boundary junction with different morphology of titanium carbides. Reprinted from Ref 107, Copyright 2016, with permission from Elsevier

to the second phase strengthening provided by carbide particles, which inhibit the dislocation motion in the matrix. A comparison work between this alloy and the same compo-

sition plus 0.2%C content was performed showing a coarse β-phase equiaxed structure with a grain size of around 110 μm and some α phase in the matrix and the grain boundaries (Ref 108).

These two previous micrographs showed Ti carbides embedded in two different Ti matrixes. By LPBF processing this material, it hypothetically might be experienced a combination of these two matrixes or one of the two can be the preferable matrix to be dominant in the final microstructure. There is not enough background in the literature on this statement. Thermal or mechanical post-processing may also induce a specific microstructural development.

4.5.3 Properties. V and Cr both act as solid solution strengthener. However, V serves as the major β stabilizer. The presence of C in some compositions of this alloy may cause the formation of carbonitrides due to its low solubility. The improvement of mechanical performance is commonly based on the addition of Si and C, according to Ref 109. The properties of the alloy are declared to be exceptional, according to the developer. However, they can also be improved by adding relatively small amounts of alloying elements (Ref 106). Burn resistance is one of the most important properties of this alloy. It is important to declare how to define the burn resistance definition because it is a function of the type of test and test parameters (Ref 35, 110). Some prospective alloying elements for improving the alloy performance (burning resistance, oxidation resistance, creep resistance, mechanical strength) and their proposed range of use are shown in Table 13 (Ref 106).

Particularly, the existence of C has been demonstrated to improve the post-creep ductility of Alloy C without affecting its tensile ductility at room temperature. However, an excess of C (more than 0.05%) may results in the formation of carbides, as suggested by Sun and Lavernia (Ref 109). These phases are normally quite hard and strong but have little ductility (Ref 106). Temperature increasing also influences the behavior of elastic modulus, shear modulus and some thermal properties.

Table 13 Prospective quaternary alloying elements for Alloy C enhancement (Ref 106)

	Broad	Preferred
B	0-0.6	0.1-0.5
Be	0-0.4	0.1-3.0
C	0-2.5	0.01-2.0
Co	0-7.0	0.5-6.0
Cr	0-7.0	0.5-6.0
Fe	0-4.0	0.5-3.0
Mn	0-7.0	0.5-5.0
Mo	0-12	0.5-10.0
Nb	0-12	0.5-10.0
Ni	0-12	0.5-10.0
O	0-0.3	0.08-0.2
Re	0-1.5	0.01-1.0
Si	0-2.5	0.01-2.0
Sn	0-2.5	0.1-2.0
Ta	0-1.5	0.1-1.0
W	0-2.5	0.5-2.0
Zr	0-5.0	0.5-4.0
Bi	0-1.5	0.1-1.0
Ga	0-2.5	0.1-2.0
Hf	0-1.5	0.1-1.0

Elastic and shear moduli slightly decrease as temperature increases, whereas specific heat, thermal expansion, thermal conductivity and thermal diffusivity increase as temperature increase as well (Ref 111). Unambiguously, the specific heat of this alloy increases linearly from 565 to 677 J/(kg K). It has also been reported that this specific heat is higher than that of Ti64 and pure Ti.

In the biomedical field, Ti-Nb alloys are promising. It may make them as potential materials to be used for medical devices fabrication. Different constituent elements make it suitable for specific applications, but their processability via LPBF is under investigation, considering the microstructural evolution and its impact on the mechanical performance of scaffold structures mainly. Different recent results of this metallurgical system—considering the differences upon adding other constituent elements—are discussed in the section below.

4.6 Ti-Nb System

Ti-Nb alloys are also considered as βTi-alloys. They have high strength but low Young's modulus. This is also combined with excellent biocompatibility, shape memory property, superelasticity and outstanding corrosion resistance. This Ti composition is considered as promising material for biomedical applications (Ref 112-115). Nevertheless, Ti2448 takes the lead for manufacturing medical implants because of its lower Young's modulus—as compared to Ti-Nb alloys—and good balance with high strength. In the last years, Ti-Nb system has been systematically studied considering minor additions of Zr, Sn and Ta.

The work reported in Ref 116 was focused on analyzing the anisotropic microstructure and mechanical properties of Ti-13Nb-13Zr processed via LPBF. Among the obtained results, there were found long and thin prior-β columnar grains which were developed along the building direction. It was observed higher microhardness in the horizontal direction than in the vertical direction on specific specimens under certain processing conditions. The preferentially oriented prior-β grains in longitudinal direction resulted in the anisotropic tensile elongation properties. Also, with Ref 116, the work in Ref 117 studied the same composition but focused on texture evolution, phase transformation and mechanical performance. They were able to control the crystallographic texture orientation and phase transformation for the first time by LPBF implementing different scanning strategies. They were defined according to variations on the track angles inside layers (0°, 45° and 90°) and chessboard scanning. Preferential growth directions of the columnar cells along building directions were detected for 0° and 90°. The content of the constituent phases (α′ and β) was also detected to be dependent on the scanning strategy. Between these two phases, the α′-phase has a higher elastic modulus than the β-phase. The results of nanoindentation tests revealed (in indentation load versus penetration depth plot) higher hardness and better wear resistance than the commercially used Ti.

Upon adding Zr and Ta to the Ti-Nb metallurgical system, Zhou et al. (Ref 118) investigated the processing of Ti-35Nb-7Zr-5Ta via LPBF looking for an optimized set of parameters for obtaining densified bulk samples. The single-track routine was used to study the combination between the laser power and the scanning speed. Continuous and uniforms tracks were achieved with a power about of 130 W and scanning speed about 0.6 m/s. It was observed that the microstructure obtained

with such optimized parameters presented melt pool boundaries related to microsegregation. Also, a coarse columnar grain structure was detected in perfect alignment with the building direction. It was expected to result in considerably better mechanical properties anisotropy. The mechanical performance of the samples was evaluated through Vickers microhardness and compression tests. It was also considered the effect of porosity on mechanical properties.

In the study (Ref 119), Ti-33Nb-4Sn was evaluated upon studying its microstructure and mechanical properties. The analysis was performed through additive manufactured porous scaffolds for orthopedic applications. Two porous scaffolds (diamond and rhombic dodecahedron) fabricated by LPBF were used. Microstructure, defects characteristics and phase were investigated and correlated considering the effect of pore structure, processing parameters and unit cell. Both porous scaffolds showed good formability without apparent deformation and collapse of the struts. Some discontinuities and holes were observed at the intersection of the struts of rhombic dodecahedron structures. Fine β-phase dendrites were observed as a result of the rapid solidification, which is consequence of the high cooling rates of the LPBF process. The marked difference in the melting point of Nb and Sn lead to segregation of *Sn* and the formation of unmelted Nb particles during solidification. There were also observed some small holes generated by evaporation of Sn. The compressive and bending strength of the samples decrease with the decrease of strut sizes. It was associated with the presence of defects such as segregation of Sn, balling and presence of unmelted Nb. Between both scaffolds structures, it was evidenced that the diamond structure samples always showed better mechanical performance than those of the dodecahedron structure samples upon considering the same unit cell size.

Another composition of this metallurgical system was analyzed by Cheng et al. (Ref 120). This time, it was studied the Ti-35Zr-28Nb alloy and its mechanical performance. Different porosity values were also analyzed in two different scaffold configurations (FCCZ and FBCCZ) upon printing scaffold structures via LPBF. It was determined elastic modulus values and compressive yield strength values. The porosity of the FBCCZ was significantly lower than that of the designed porosity. It was attributed to more partially melted metal particles deposited on the surfaces of the struts inside the porous structure.

Conventional specimens of Ti-35Nb-7Zr-5Ta were fabricated through LPBF and analyzed by Li et al. (Ref 121). Similarly with Ref 118, it was found that the single β-phase leads to excellent mechanical properties which favor this composition for biomedical applications. A high density value was found at 150 J/mm^3 with a tensile strength of about 630 MPa and a low elastic modulus of about 80 GPa. The observed microstructure was found to be composed of fine, equiaxed, as well as narrow elongated grains along the laser tracks. A high amount of local strains were concluded to be responsible for the excellent mechanical strength found after the tests. These local strains were the result of rapid cooling and a high density of dislocation network. In general terms, the good ductility, low modulus and remarkable strength of Ti-35Nb-7Zr-5Ta processed via LPBF make it an ideal material for load-bearing biomedical applications.

The work of Ref 122 studied the Ti-Nb system with a similar-in-constituents powder as the composition of Ref 116 but different stoichiometrically. A unique microstructure in terms of strong texture and strain-induced martensitic transformation was observed. A hard-wraps-soft texture was also observed, which makes the LPBF produced parts more ductile than conventional hot-rolled counterpart. This texture was also observed in the work of Ref 71 with similar results. The formation of sub-grain boundaries, sub-grains and columnar grains were found to be responsible for an increasing of yield strength and ultimate tensile strength. The comparison work reported thin prior-β columnar grains along the building direction. However, the processing conditions are quite different and, therefore, such structures are far from being comparable. In the work of Ref 123, the superelastic response of Ti-35Nb-2Ta-3Zr was studied with scaffolds produced via LPBF. It was found an influence of the scaffold pores size in the superelastic properties and the strain recovery during deformation. The Young's modulus of the scaffolds with different pore sizes was found to be favorable for biomedical bone implants due to its closeness with the one of human bone. Microstructurally, similar results comparing to Ref 61 (in which the same composition was investigated) were found. Several transformation mechanisms like stress-induced and twinning-induced, and martensitic transformation were also reported.

By elemental powder mixing, Ti-35Nb was investigated in the work of Ref 124. Starting from the uncertainty about the chemical homogeneity and the resultant microstructures of the printed parts via LPBF, the mechanical properties and final microstructure were studied. Some microstructural inhomogeneity was observed because of undissolved Nb particles. It was revealed that such particles deteriorated the macroscopic plastic deformability of the as-built samples. Heat treatment was also found to be beneficial for homogeneity improvement in both chemical composition and microstructure. As a consequence of the mechanical stability of Ti-Nb β phase, the mechanical response was found to be enhanced. Dendritic β grains were also observed. Because of it, the as-built Ti-35Nb showed relatively high tensile strength, but ductility was evidenced to be low. A work performed with premixed powders (Ti-Cr based alloy) (Ref 125) reported also promising results between density and energy density.

Table 14 summarizes the main findings of the reviewed metallographic systems:

5. Time Evolution of Related Works of the Selected Beta Phase Titanium Alloys

βTi-alloys have been investigated from different processing conditions, but most of the results are focused on these alloys processed conventionally. The number of research works that have been published, which are available in the literature, is shown in Fig. 9. On the one hand, Fig. 10 shows the number of works—per country worldwide—of the βTi-alloys processed via LPBF. Research works of Alloy C processed via LPBF are not reported yet, as was stated in subsection 4.5.1.

6. Future Outlook

• Further research about LBPF parameters tuning must be

Table 14 Summary of findings of processability, phase transformation and microstructure, and properties of the reviewed metallurgical systems

Processability	**Ti2448** A combination of high energy density and low scanning speed values lead to high density values, decreasing strength and low relative porosity. Low scanning speeds (only) make density decrease keeping the hardness at high values. Low energy density promotes presence of Nb unmelted particles, which affects ductility, facilitating crack propagation. High scanning speeds promote molten pool instability, balling, poor surface finishes and dross formation
	Ti1023 Scarce information is available of Ti1023 processed via LPBF. The development of fine β columnar grains and widespread cell structures can be observed upon printing with a small powder layer thickness, a low laser power and a short exposure time (low energy density). Low energy density can also promote an anisotropic behavior of plasticity. On the contrary, at high energy density, grain growth and texture increasing can be observed with a decrease in cell structures
	Ti5553 This alloy indicates a larger LPBF processing window and a higher working strength than Ti1023. Ti5553 is characterized by a demonstrated weldability. The energy density must be carefully tuned to have the optimal grain size distribution to achieve high material density. The processability of this material was confirmed based on relatively good values obtained from different processing conditions
	Beta C This is one of the Ti-alloys that can be solution-treated at T_β. Typically, the range of temperature for solution treatment is between 790 and 925 °C, time between 0.5 and 1.0 h, followed by either water quenching, air cooling or forced air cooling depending on the section size. Few related works appear reported in the literature of this composition processed via metal AM
	Alloy C Related works of Alloy C processed via LPBF are not reported in the literature. This alloy was developed to be a non-combustible material for aeronautical applications. A ternary system Ti-V-Cr like this satisfies the non-susceptibility to sustained combustion and resistance to excessive temperatures and stresses. This alloy also provides a significant weight-save as compared to nickel-based superalloys
	Ti-Nb System A high density value was found at 150 J/mm^3 with a tensile strength of about 630 MPa and a low elastic modulus of about 80 GPa when Ti-35Nb-7Zr-5Ta was processed via LPBF. However, a more general concept on this regard cannot be given because of the influence of constituents of different compositions that can be acceptable in this metallurgical system
Phase transformation and microstructure	**Ti2448** Interstitial oxygen can improve the stabilization of β phase. The constituent phases of this alloy are based on β-phase mainly, but it could be accompanied by metastable phases ω and α''. The formation of a microstructure with a monolithic β phase allows decreasing the elastic modulus of this alloy. Compressive strength and elastic modulus can increase after a solution and aging heat treatment
	Ti1023 Phase transformations such as $\beta \rightarrow \alpha''$ martensitic transformation, athermal or isothermal $\beta \rightarrow \omega$ and $\beta \rightarrow \alpha$ transformation can be present. The phase transformation $\beta \rightarrow \alpha''$ could be induced by stress, including internal stresses arising from quenching and external stresses such as tensile loading or mechanical polishing
	Ti5553 Precipitation of the α-phase can occur in the vicinity of the heat-affected zone (HAZ), which typically reaches temperatures close to T_β. The dissolution of preexisting base metal α-phase precipitates can occur near to HAZ when T_β is exceeded. The extent of these phase transformations depends on the cooling rates and thermal history of the part being processed. It can be possible, differently than other Ti-alloys, to produce a range of microstructures with different morphologies and ratios of both α and β phases
	Beta C In the solution annealed condition, Beta C shows a microstructure that consists of a metastable β phase, which is readily retained at common section sizes by air cooling or water quenching. Based on the thermomechanical processing history and the section size, the β grain size varies. In the STA condition, increases in the strength in the order of 40% can be obtained by precipitation strengthening. Upon LPBF processing this alloy, a fully β microstructure with grains elongated in the building direction can be obtained. This microstructure resulted in low strength, but relatively high ductility and fracture toughness compared to Ti64 also processed via LPBF
	Alloy C The evolution of the microstructure of this alloy has not been studied deeply. The microstructure after cast processing basically consists of recrystallized equiaxed β-phase, some small volume fractions of titanium carbides and α-phase. Based on the equilibrium of ternary systems, titanium carbides are expected to precipitate within the α phase. The addition of carbon in this composition also showed increasing in creep resistance. This was attributed to the second particle strengthening of carbide particles, which inhibit the dislocation motion in the matrix
	Ti-Nb System Long and thin prior-β columnar grains along building direction can be found. It can result in anisotropic tensile elongation properties. Constituent phases (α' and β) can be detected to be dependent on the scanning strategy. Between these two phases, the α'-phase has higher elastic modulus than that of the β-phase. Fine β-phase dendrites can be obtained as a result of the rapid solidification which is a consequence of the high cooling rates of the LPBF process.

Table 14   continued

Properties	**Ti2448** Good balance of low modulus/high strength ratio, superelasticity properties and non-presence of toxic elements for human body. Regular values of Young's modulus, S_y and UTS of this alloy processed by LPBF are about 53 GPa, 570 and 670 MPa, respectively
	Ti1023 Volume fraction, grain orientation, grain size and phase morphology of β-phase, α' and α'' phases have also been largely associated as strong features that influence the mechanical properties in Ti1023. The α-phase content does not significantly influence on the mechanical properties of Ti1023 after heat treatment. The morphology evolution of phases can be associated with the behavior of yield point and impact strain
	Ti5553 High ductility with low as-built hardness is typical on Ti5553 as compared to Ti64. This alloy composition can strengthen via both solid solution mechanisms in the single phase and precipitation strengthening of α-phase at temperatures below the T_β around 850 °C. Material densities of about 99.93% can be achieved by selecting an optimized value of energy density. However, it finally depends on the geometry of the component to be printed, and the inherent features of powdered material like the atomization process, particle size distribution, morphology and initial porosity if it applies
	Beta C Through a precipitation strengthening mechanism, increases in strength in the order of 40% can be possible to obtain as mentioned in the previous section. This alloy can be stress relieved in the range of (705-760 °C) for (10-60 min). The best combination of ductility and strength was observed with large type 2α precipitates formed in the β matrix upon aging above 500 °C. Variations on this composition by adding silicon also showed improvements in creep resistance and inhibition of β grain growth of the alloy. However, the addition of high amounts of silicon negatively affects the ductility of Ti-alloys at room temperature
	Alloy C The presence of carbon in some compositions of this alloy may cause the formation of carbonitrides due to its low solubility. The properties of the alloy are declared to be exceptional, according to the developer. However, they can also be improved by adding relatively small alloying elements. Burn resistance is one of the most important properties of this alloy. It is important to declare how to define the burn resistance definition because it is a function of the type of test and test parameters
	Ti-Nb System Coarse columnar grain structure can influence on considerable better mechanical properties anisotropy. Heat treatment was also found to be beneficial in this system for homogeneity improvement in both chemical composition and microstructure. As a consequence of the mechanical stability of Ti-Nb β phase, the mechanical response was found to be enhanced. Dendritic β grains were also observed. Because of it, the as-built Ti-35Nb showed relatively high tensile strength but ductility was evidenced to be low.

performed in order to adjust the allowable range of surface roughness that characterizes a good surface quality towards a better fatigue performance of lattice structures.

- Better control of homogeneity in microstructure at lattice struts level must be tailored in order to have a better mechanical response individually when a lattice structure behaves as a whole under loading conditions.
- Processability via LPBF of Alloy C must be investigated at all. This composition has not been studied before and its applicability in aeronautical application encompasses a wide range.

7. Conclusions

- The processability of βTi-alloys via LPBF has not been investigated deeply until now despite the wide application of this family of alloys in many fields of industry like aeronautical and biomedical. Because of the lack of knowledge and understanding of the LPBF processing of these alloys, reliable sets of optimal processing parameters are not known. These two fields of applications are the ones with more applicability of β-phase Ti-alloys processed via LPBF. The applications through LPBF developed in these fields industry are still being performed with different alloy compositions like Ti64.

- Ti2448 has the potential to be used in biomedical applications because of its low toxicity and low Young's modulus. Based on these two critical features (for the biomedical context), this composition tends to be preferable in the biomedical industry than the Ti64. However, there have been few research works—around 7% of the total reported works—of microstructure and mechanical behavior of this composition through LPBF processing. This fact does not allow us to understand its adequate processability for a tailored mechanical behavior as a function of the corresponding microstructure by now. Moreover, this lack of knowledge does not allow a complete implementation of Ti2448 in the biofield.
- Based on the literature review, Alloy C has not been used for processing via LPBF. This composition has excellent mechanical performance in terms of high oxidation and creep resistance and outstanding mechanical strength. Its features also provide weight savings as compared to nickel superalloys. Its LPBF processability must be addressed to place the composition at hand on high-performance applications in the aerospace field where its non-burning features are required.
- The LPBF processability of Ti5553, Ti1023 and Beta C and their associated microstructures and mechanical behaviors have been scarcely investigated. Around 12% of the total reported works of β-phase Ti-alloys—without considering Ti2448—are focused on these three compositions. They are characterized by being attractive materials for structural applications in the aeronautical field. The versatility given by LPBF process for producing topologi-
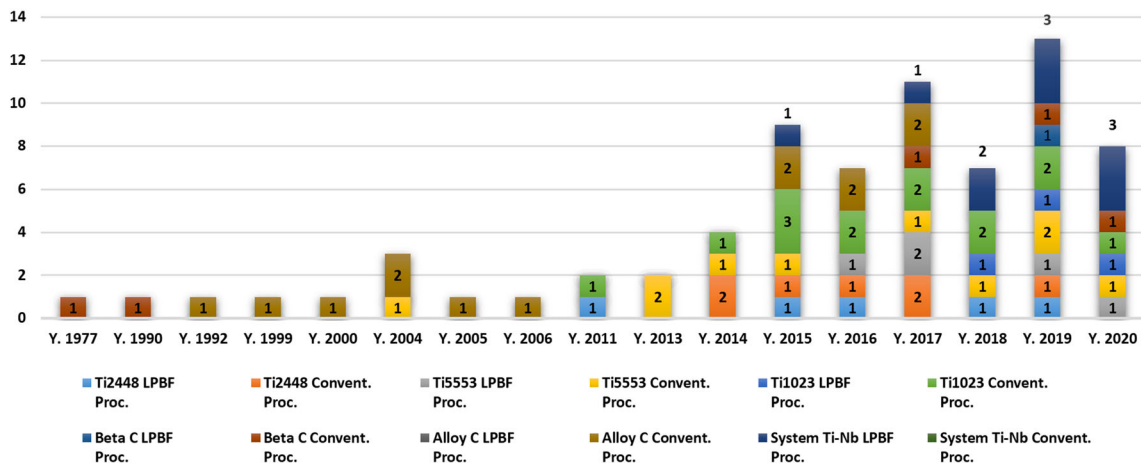
Fig. 9. Research works per year per material and manufacturing processing method. These works are focused on microstructure and mechanical behavior when processed via LPBF and conventionally processed for different study goals.
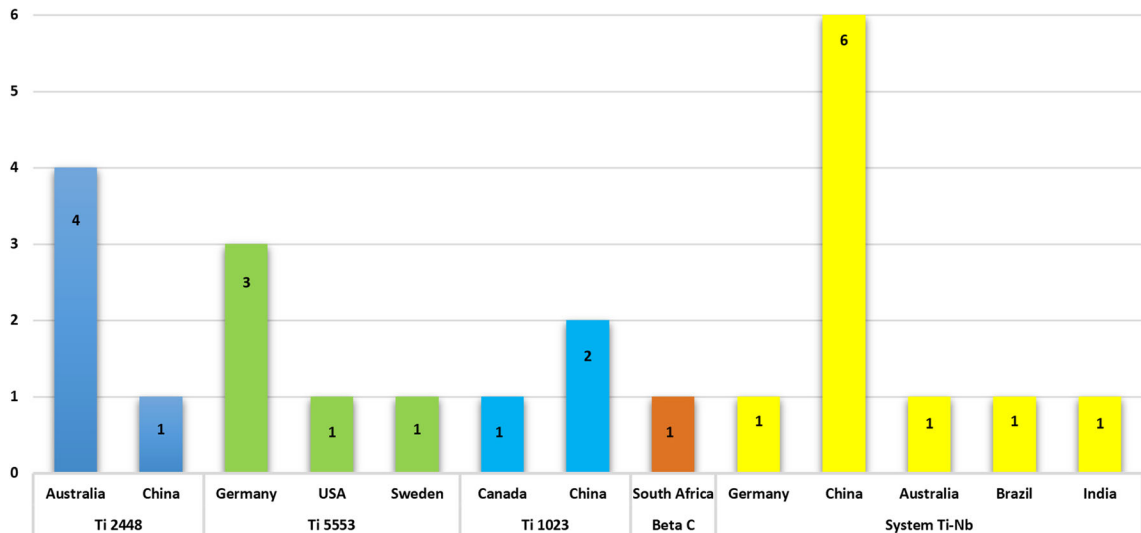

Fig. 10. Number of works performed on each material processed via LPBF by countries focused on microstructure and mechanical behavior

cally optimized structures makes imperative the need to expand the use of these three compositions for processing via LPBF. Metallurgy of them based on conventional processability is well known and its consideration as a starting point is valuable.

- Most-known Ti-alloys, such as Ti64, are still taken as a starting point for understanding how the inherent metallurgical features (like grain size and orientation, phase distribution, their morphology and volume fractions), have a direct influence on the final microstructure and the desired mechanical properties. The relationship between these last two material entities is tightly linked to the mechanical behavior of the material and the functional performance of the component manufactured via LPBF when in service.

- The Ti-Nb metallurgical system is highly promising for biomedical applications considering its low Young's modulus. However, the role of the other constituents—like Sn, Zr and Ta—in the final mechanical performance must be

carefully understood for tailoring the appropriate mechanical response based on the final application in the biomedical field. Even, the amount of Nb should not be underestimated considering that this constituent is prone to segregation which negatively affects the kinetic equilibrium of the grain boundaries.

- The interest in researching on βTi-alloys has been increasing, starting at the beginning of the last decade because of the new developments in the aeronautical and biomedical industry. More efficient combustion engine components, lighter-weight structural elements and consolidated subsystems—to be topologically optimized and produced via metal AM—that replace conventionally assembled multiparts in the aeronautical industry demand the implementation of alloy compositions with the optimized material response, which is evidenced in the enhanced mechanical performance. Besides that, the processability of such compositions via LPBF—which allows building the optimized

topologically components—must be known and fully understood.

Acknowledgments

Funding

References

1. H.E. Sabzi, Powder Bed Fusion Additive Layer Manufacturing of Titanium Alloys, *Mater. Sci. Technol.*, 2019, **35**, p 875–890
2. G. Mert, *Optimization of the Mechanical Properties of Ti-6Al-4V Alloy Produced by Three Dimensional Additive Manufacturing Using Thermomechanical Processes*, Ankara, TU, 2017
3. I. Gibson, D. Rosen, and B. Stucker, *Additive Manufacturing Technologies*, Springer, New York, 2015
4. D. Gu, *Laser Additive Manufacturing of High-Performance Materials*, Springer, New York, 2015
5. W. Frazier, Metal Additive Manufacturing: A Review, *J. Mater. Eng. Perform.*, 2014, **23**, p 1917–1928
6. W.J. Sames, F.A. List, S. Pannala, R.R. Dehoff, and S.S. Babu, The Metallurgy and Processing Science of Metal Additive Manufacturing, *Int. Mater. Rev.*, 2016, **61**, p 315–360
7. D. Herzog, V. Seyda, E. Wycisk, and C. Emmelmann, Additive Manufacturing of Metals, *Acta Mater.*, 2016, **117**, p 371–392
8. H. Ali, H. Ghadbeigi, and K. Mumtaz, Processing Parameter Effects on Residual Stress and Mechanical Properties of Selective Laser Melted Ti6Al4V, *J. Mater. Eng. Perform.*, 2018, **27**, p 4059–4068
9. R.P. Kolli and A. Devaraj, A Review of Metastable Beta Titanium Alloys, *Met. MDPI*, 2018, **8**, p 1–41
10. M. Markl and C. Körner, Multi-Scale Modeling of Powder-Bed-Based Additive Manufacturing, *Annu. Rev. Mater. Res.*, 2016, **46**, p 1–34
11. C.Y. Yap, C.K. Chua, Z.L. Dong, Z.H. Liu, D.Q. Zhang, L.E. Loh, and S.L. Sing, Review of Selective Laser Melting: Materials and Applications, *Appl. Phys. Rev.*, 2015, **2**, p 1–21
12. X. Zhang, C. Yocom, B. Mao, and Y. Liao, Microstructure Evolution during Selective Laser Melting of Metallic Materials: A Review, *J. Laser Appl.*, 2019, **31**, p 1–19
13. W. King, A. Anderson, R. Ferencz, N. Hodge, C. Kamath, S. Khairallah, and A. Rubenchik, Laser Powder Bed Fusion Additive Manufacturing of Metals; Physics, Computational, and Materials Challenges, *Appl. Phys. Rev.*, 2015, **2**, p 1–26
14. T. DebRoy, H.L. Wei, J.S. Zuback, T. Mukherjee, J.W. Elmer, J.O. Milewski, A.M. Beese, A. De Wilson-Heid, A., and W. Zhang, Additive Manufacturing of Metallic Components—Process, Structure and Properties, *Prog. Mater. Sci.*, 2018, **92**, p 112–224
15. A. Leicht, *Aspects of Building Geometry and Powder Characteristics in Powder Bed Fusion*, Dept. of Industrial and Materials Science. Chalmers University of Technology, Gothenburg, 2018
16. T. Mishurova, K. Artzt, J. Haubrich, G. Requena, and G. Bruno, New Aspects About the Search for the Most Relevant Parameters Optimizing SLM Materials, *Addit. Manuf.*, 2019, **25**, p 325–334
17. J. Yang, H. Yu, J. Yin, M. Gao, Z. Wang, and X. Zeng, Formation and Control of Martensite in Ti-6Al-4V Alloy Produced by Selective Laser Melting, *Mater. Des.*, 2016, **108**, p 308–318
18. C. Li, J.F. Liu, X.Y. Fang, and Y.B. Guo, Efficient Predictive Model of Part Distortion and Residual Stress in Selective Laser Melting, *Addit. Manuf.*, 2017, **17**, p 157–168
19. J. Ning, E. Mirkoohi, Y. Dong, D. Sievers, H. Garmestani, and S.Y. Liang, Analytical Modeling of 3D Temperature Distribution in Selective Laser Melting of Ti-6Al-4V Considering Part Boundary Conditions, *J. Manuf. Process.*, 2019, **44**, p 319–326
20. T. Yu, M. Li, A. Breaux, M. Atri, S. Obeidat, and C. Ma, Experimental and Numerical Study on Residual Stress and Geometric Distortion in Powder Bed Fusion Process, *J. Manuf. Process.*, 2019, **46**, p 214–224
21. T. Tancogne-Dejean and D. Mohr, Elastically-Isotropic Elementary Cubic Lattices Composed of Tailored Hollow Beams, *Extreme Mech. Lett.*, 2018, **22**, p 13–18
22. Y. Sha, L. Jiani, C. Haoyu, R.O. Ritchie, and X. Jun, Design and Strengthening Mechanisms in Hierarchical Architected Materials Processed Using Additive Manufacturing, *Int. J. Mech. Sci.*, 2018, **149**, p 150–163
23. J. Fiocchi, C.A. Biffi, D. Scaccabarozzi, B. Saggin, and A. Tuissi, Enhancement of the Damping Behavior of Ti6Al4V Alloy through the Use of Trabecular Structure Produced by Selective Laser Melting, *Adv. Eng. Mater.*, 2020, **22**, p 1–6
24. C. Li, H. Lei, Z. Zhang, X. Zhang, H. Zhou, P. Wang, and D. Fang, Architecture Design of Periodic Truss-Lattice Cells for Additive Manufacturing, *Addit. Manuf.*, 2020, **34**, p 1–15
25. V. Challis, X. Xu, L.C. Zhang, A.P. Roberts, J.F. Grotowski, and T.B. Sercombe, High Specific Strength and Stiffness Structures Produced Using Selective Laser Melting, *Mater. Des.*, 2014, **63**, p 783–788
26. Y.J. Liu, S.J. Li, L.C. Zhang, Y.L. Hao, and T.B. Sercombe, Early Plastic Deformation Behaviour and Energy Absorption in Porous β-Type Biomedical Titanium Produced by Selective Laser Melting, *Scr. Mater.*, 2018, **153**, p 99–103
27. Y.J. Liu, H. Wang, S.J. Li, W.J. Wang, W.T. Hou, Y.L. Hao, R. Yang, and L.C. Zhang, Compressive and Fatigue Behavior of Beta-Type Titanium Porous Structures Fabricated by Electron Beam Melting, *Acta Mater.*, 2017, **126**, p 58–66
28. Z.H. Jiao, R.D. Xu, H.C. Yu, and X.R. Wu, Evaluation on Tensile and Fatigue Crack Growth Performances of Ti6Al4V Alloy Produced by Selective Laser Melting, *Struct. Integr. Procedia*, 2017, **7**, p 124–132
29. C.A. Biffi, J. Fiocchi, E. Ferrario, A. Fornaci, M. Riccio, M. Romeo, and A. Tuissi, Effects of the Scanning Strategy on the Microstructure and Mechanical Properties of a TiAl6V4 Alloy Produced by Electron Beam Additive Manufacturing, *Int. J. Adv. Manuf. Technol.*, 2020, **107**, p 4913–4924
30. C.A. Biffi, P. Bassani, J. Fiocchi, and A. Tuissi, Microstructural and Mechanical Response of NiTi Lattice 3D Structure Produced by Selective Laser Melting, *Met. MDPI*, 2020, **10**, p 1–9

31. Y. Liu, S. Li, W. Hou, S. Wang, Y. Hao, R. Yang, T.B. Sercombe, and L. Zhang, Electron Beam Melted Beta-Type Ti-24Nb-4Zr-8Sn Porous Structures with High Strength-to-Modulus Ratio, *J. Mater. Sci. Technol.*, 2016, **32**, p 505–508

32. S. Zhao, S.J. Li, S.G. Wang, W.T. Hou, Y. Li, L.C. Zhang, Y.L. Hao, R. Yang, R.D.K. Misra, and L.E. Murr, Compressive and Fatigue Behavior of Functionally Graded Ti-6Al-4V Meshes Fabricated by Electron Beam Melting, *Acta Mater.*, 2018, **150**, p 1–15

33. Y.J. Liu, D.C. Ren, S.J. Li, H. Wang, L.C. Zhang, and T.B. Sercombe, Enhanced Fatigue Characteristics of a Topology-Optimized Porous Titanium Structure Produced by Selective Laser Melting, *Addit. Manuf.*, 2020, **32**, p 1–10

34. S. Singamneni, Y. Lv, A. Hewitt, R. Chalk, W. Thomas, and D. Jordison, Additive Manufacturing for the Aircraft Industry: A Review, *J. Aeronaut. Aerosp. Eng.*, 2019, **8**, p 1–13

35. J. Cotton, R. Briggs, R. Boyer, S. Tamirisakandala, P. Russo, N. Shchetnikov, and J. Fanning, State of the Art in Beta Titanium Alloys for Airframe Applications, *JOM Miner. Met. Mater. Soc.*, 2015, **67**, p 1281–1303

36. D.J. Horst, C.A. Duvoisin, and R. de Almeida Vieira, Additive Manufacturing at Industry 4.0: a Review, *Int. J. Eng. Tech. Res. (IJETR)*, 2018, **8**, p 3–8

37. D. Renzo, E. Sgambitterra, P. Magarò, F. Furgiuele, C. Maletta, C. A. Biffi, J. Fiocchi, and A. Tuissi, Multiaxial Fatigue Behavior of Additively Manufactured Ti6Al4V Alloy: Axial–Torsional Proportional Loads, *Mat. Des. Process.*, 2020, p 1–10

38. L.C. Zhang and H. Attar, Selective Laser Melting of Titanium Alloys and Titanium Matrix Composites for Biomedical Applications: A Review, *Adv. Eng. Mater.*, 2016, **18**, p 463–475

39. S. Ghouse, S. Babu, R. Van Arkel, K. Nai, P. Hooper, and J. Jeffers, The Influence of Laser Parameters and Scanning Strategies on the Mechanical Properties of a Stochastic Porous Material, *Mater. Des.*, 2017, **131**, p 498–508

40. S. Liu and Y.C. Shin, Additive Manufacturing of Ti6Al4V Alloy: A Review, *Mater. Des.*, 2019, **164**, p 1–23

41. L.C. Zhang, H. Attar, M. Calin, and J. Eckert, Review on Manufacture by Selective Laser Melting and Properties of Titanium Based Materials for Biomedical Applications, *Mater. Technol. Adv. Perform. Mater.*, 2016, **31**, p 66–76

42. L.C. Zhang and L.Y. Chen, A Review on Biomedical Titanium Alloys: Recent Progress and Prospect, *Adv. Eng. Mater.*, 2019, **21**, p 1–29

43. S. Singh and S. Ramakrishna, Biomedical Applications of Additive Manufacturing: Present and Future, *Curr. Opin. Biomed. Eng.*, 2017, **2**, p 101–115

44. C. Leyens and M. Peters, *Titanium and Titanium Alloys*, WILEY-VCH Verlag GmbH & Co. KGaA, Köln, 2003

45. F.F. Schmidt and R.A. Wood, *Technical Memorandum: Heat Treatment of Titanium and Titanium Alloys*, Marshall Space Flight Center-Nasa, Huntsville, 1966

46. M.J. Donachie, *Titanium: A Technical Guide*, 2nd ed. ASM International, Novelty, 2000

47. F.H. Froes, P.G. Allen, and M. Niinomi, *Non-Aerospace Applications of Titanium*, The Minerals, Metals & Materials Society, Pennsylvania, 1998

48. A. Mouritz, *Introduction to Aerospace Materials*, Woodhead Publishing Limited, Cambridge, 2012

49. D. Laughlin and K. Hono, *Physical Metallurgy*, 5th ed. Elsevier, Amsterdam, 2014

50. P. Barriobero-Vila, G. Requena, F. Warchomicka, A. Stark, N. Schell, and T. Buslaps, Phase Transformation Kinetics during Continuous Heating of a β-Quenched Ti-10V-2Fe-3Al Alloy, *Mater. Sci.*, 2015, **50**, p 1412–1426

51. C.A. Biffi, J. Fiocchi, F. Valenza, P. Bassani, and A. Tuissi, Selective Laser Melting of NiTi Shape Memory Alloy: Processability, Microstructure, and Superelasticity, *Shape Mem. Superelast.*, 2020, **6**, p 342–353

52. M. Niinomi and M. Nakai, Titanium-Based Biomaterials for Preventing Stress Shielding between Implant Devices and Bone, *Int. J. Biomater.*, 2011, **2011**, p 1–10

53. M. Niinomi, M. Nakai, and J. Hieda, Development of New Metallic Alloys for Biomedical Applications, *Acta Biomater.*, 2012, **8**, p 3888–3903

54. H.X. Yang, S.J. Li, W.T. Hou, Y.L. Hao, R. Yang, and R.D.K. Misra, Recoverable Strain in a New Biomedical Ti-24Nb-4Zr-8Sn Alloy with Cellular Structure Fabricated by Electron Beam Melting, *Mater. Technol.*, 2020, **35**, p 881–886

55. T. Ishimoto, K. Hagihara, K. Hisamoto, S.H. Sun, and T. Nakano, Crystallographic Texture Control of Beta-Type Ti–15Mo–5Zr–3Al Alloy by Selective Laser Melting for the Development of Novel Implants with a Biocompatible Low Young's Modulus, *Scr. Mater.*, 2017, **132**, p 34–38

56. J. Martins, R. Oliveira, R. Nogueira, and C. Grandini, Internal Friction and Microstructure of Ti and Ti-Mo Alloys Containing Oxygen, *Arch. Metall. Mater.*, 2016, **61**, p 25–30

57. L. Qi, K. Zhang, X. Qiao, L. Huang, X. Huang, and X. Zhao, Microstructural Evolution in the Surface of Ti-10V-2Fe-3Al Alloy by Solution Treatments, *Prog. Natural Sci. Mater. Int.*, 2020, **30**, p 106–109

58. H. Ba, L. Dong, Z. Zhang, and X. Lei, Effects of Trace Si Addition on the Microstructures and Tensile Properties of Ti-3Al-8V-6Cr-4Mo-4Zr Alloy, *Metals*, 2017, **7**, p 1–8

59. T. Nagase, T. Hori, M. Todai, S.H. Sun, and T. Nakano, Additive Manufacturing of Dense Components in Beta-Titanium Alloys with Crystallographic Texture from a Mixture of Pure Metallic Element Powders, *Mater. Des.*, 2019, **173**, p 1–10

60. W. Chen, C. Chen, X. Zi, X. Cheng, X. Zhang, Y.C. Lin, and K. Zhou, Controlling the Microstructure and Mechanical Properties of a Metastable β Titanium Alloy by Selective Laser Melting, *Mater. Sci. Eng. A*, 2018, **726**, p 240–250

61. N. Hafeez, S. Liu, E. Lu, L. Wang, R. Liu, W. Lu, and L.C. Zhang, Mechanical Behavior and Phase Transformation of β-type Ti-35Nb-2Ta-3Zr Alloy Fabricated by 3D-Printing, *J. Alloys Compd.*, 2019, **790**, p 117–126

62. R.P. Kolli, W. Joost, and S. Ankem, Phase Stability and Stress-Induced Transformations in Beta Titanium Alloys, *Miner. Met. Mater. Soc.*, 2015, **67**, p 1–8

63. V.V. Balasubrahmanyam and Y.V.R.K. Prasad, Hot Deformation Mechanisms in Metastable Beta Titanium Alloy Ti-10V-2Fe-3Al, *Mater. Sci. Technol.*, 2013, **17**, p 1–8

64. I. Polmear, D. St. John, F.G. Nie, and M. Qian, Titanium Alloys, *Light Alloys: Metallurgy of the Light Metals*, A.C.A. Garcia, Ed., Butterworth-Heinemann, Oxford, 2017, p 369–460

65. M. Kaur and K. Singh, Review on Titanium and Titanium Based Alloys as Biomaterials for Orthopaedic Applications, *Mater. Sci. Eng. A*, 2019, **102**, p 844–862

66. F.H. Froes and M. Qian, *Titanium in Medical and Dental Applications*, Elsevier, Duxford, 2018

67. Y.J. Liu, X.P. Li, L.C. Zhang, and T.B. Sercombe, Processing and Properties of Topologically Optimised Biomedical Ti–24Nb–4Zr–8Sn Scaffolds Manufactured by Selective Laser Melting, *Mater. Sci. Eng. A*, 2015, **642**, p 268–278

68. L.C. Zhang, D. Klemm, J. Eckert, Y.L. Hao, and T.B. Sercombe, Manufacture by Selective Laser Melting and Mechanical Behavior of Biomedical Ti–24Nb–4Zr–8Sn Alloy, *Scr. Mater.*, 2011, **65**, p 21–24

69. R. Yang, Y. Hao, and S. Li, Development and Application of Low-Modulus Biomedical Titanium Alloy Ti2448, *Biomedical Engineering, Trends in Materials Science*, A. Laskovski, Ed., IntechOpen, London, 2011, p 225–248

70. Y.J. Liu, S.J. Li, H.L. Wang, W.T. Hou, Y.L. Hao, R. Yang, T. Sercombe, and L.C. Zhang, Microstructure, Defects and Mechanical Behavior of Beta-Type Titanium Porous Structures Manufactured by Electron Beam Melting and Selective Laser Melting, *Acta Mater.*, 2016, **113**, p 56–67

71. C. Yang, Z. Zhang, S. Li, Y. Liu, T. Sercombe, W. Hou, P. Zhang, Y. Zhu, Y. Hao, Z. Zhang, and R. Yang, Simultaneous Improvement in Strength and Plasticity of Ti-24Nb-4Zr-8Sn Manufactured by Selective Laser Melting, *Mater. Des.*, 2018, **157**, p 52–59

72. P. Qin, Y. Chen, Y.J. Liu, J. Zhang, L.Y. Chen, Y. Li, X. Zhang, C. Cao, H. Sun, and L.C. Zhang, Resemblance in Corrosion Behavior of Selective Laser Melted and Traditional Monolithic β Ti-24Nb-4Zr-8Sn Alloy, *ACS Biomater. Sci. Eng.*, 2019, **5**, p 1141–1149

73. Y.L. Hao, S.J. Li, S.Y. Sun, C.Y. Zheng, and R. Yang, Elastic Deformation Behaviour of Ti-24Nb-4Zr-7.9Sn for Biomedical Applications, *Acta Biomater.*, 2007, **3**, p 277–286

74. X. Li, S. Ye, X. Yuan, and P. Yu, Fabrication of Biomedical Ti-24Nb-4Zr-8Sn Alloy with High Strength and Low Elastic Modulus by Powder Metallurgy, *J. Alloys Compd.*, 2019, **772**, p 968–977

75. W.L. Liu, Y.Q. Zhang, Y.H. Jiang, and R. Zhou, Effects of Heat Treatment on Microstructure and Mechanical Properties of Ti-24Nb-4Zr-8Sn Alloy by Spark Plasma Sintering, *Chin. J. Nonferr. Met.*, 2017, **27**, p 1155–1161

76. Y.F. Yang, S.D. Luo, G.B. Schaffer, and M. Qian, Sintering of Ti-10V-2Fe-3Al and Mechanical Properties, *Mater. Sci. Eng.*, 2011, **528**, p 6719–6726

77. C. Li, J. Chen, Y.J. Ren, W. Li, J.J. He, and J.H. Chen, Effect of Solution Heat Treatment on the Stress-Induced Martensite Transformation in Two New Titanium Alloys, *J. Alloys Compd.*, 2015, **641**, p 192–200

78. P. Skubisz, Ł Lisiecki, M. Paćko, T. Skowronek, P. Micek, and T. Tokarski, Effect of High Strain Rate Beta Processing on Microstructure and Mechanical Properties of Near-β Titanium Alloy Ti-10V-2Fe-3Al, *J. Mater. Des. Appl.*, 2018, **232**, p 181–190

79. R. Bogucki, K. Mosór, and M. Nykiel, Effect of Heat Treatment Conditions on the Morphology of α Phase and Mechanical Properties in Ti-10V-2Fe-3Al Titanium Alloy, *Arch. Metall. Mater.*, 2014, **59**, p 1269–1273

80. C. Li, J. Chen, W. Li, J.J. He, W. Qiu, Y.J. Ren, J.L. Chen, and J.H. Chen, Study on the Relationship between Microstructure and Mechanical Property in a Metastable β Titanium Alloy, *J. Alloys Compd.*, 2015, **627**, p 222–230

81. X. Ma, F. Li, J. Cao, Z. Sun, Q. Wan, J. Li, and Z. Yuan, Study on the Deformation Behavior of β phase in Ti-10V-2Fe-3Al Alloy by micro-indentation, *J. Alloys Compd.*, 2017, **703**, p 298–308

82. D.B.A. Sagar, B. Vikas, B. Salaiah, N. Narasaiah, P. Jayapal, G.D.J. Ram, and M.S.K. Rao, Study of Microstructure and Mechanical Properties of Friction Welded Metastable Beta Titanium Alloy Titan 1023, *Mater. Today Proc.*, 2018, **5**, p 20760–20768

83. L. Qi, X. Qiao, L. Huang, X. Huang, and X. Zhao, Effect of Structural Stability on the Stress Induced Martensitic Transformation in Ti-10V-2Fe-3Al Alloy, *Mater. Sci. Eng.*, 2019, **756**, p 381–388

84. C. Li, X. Wu, J.H. Chen, and S. Van der Zwaag, Influence of α Morphology and Volume Fraction on the Stress-Induced Martensitic Transformation in Ti-10V-2Fe-3Al, *Mater. Sci. Eng.*, 2011, **528**, p 5854–5860

85. R.R. Boyer and R.D. Briggs, The Use of Beta Titanium Alloys in the Aerospace Industry, *J. Mater. Eng. Perform.*, 2005, **14**, p 681–685

86. C. Qiu and Q. Liu, Multi-scale Microstructural Development and Mechanical Properties of a Selectively Laser Melted Beta Titanium Alloy, *Addit. Manuf.*, 2019, **30**, p 1–13

87. Q. Liu and C. Qiu, Variant Selection of α Precipitation in a Beta Titanium Alloy during Selective Laser Melting and Its Influence on Mechanical Properties, *Mater. Sci. Eng.*, 2020, **784**, p 1–9

88. H. Azizi, H. Zurob, B. Bose, S. Reza Ghiaasiaan, X. Wang, S. Coulson, V. Duz, and A.B. Phillion, Additive Manufacturing of a Novel Ti-Al-V-Fe Alloy Using Selective Laser Melting, *Addit. Manuf.*, 2018, **21**, p 529–535

89. A.G. Illarionov, A.V. Trubochkin, A.M. Shalaev, S.M. Illarionova, and A.A. Popov, Isothermal Decomposition of β Solid Solution in Titanium Alloy Ti-10V-2Fe-3Al, *Met. Sci. Heat Treat.*, 2017, **58**, p 674–680

90. C. Zopp, S. Blümer, F. Schubert, and L. Kroll, Processing of a Metastable Titanium Alloy (Ti-5553) by Selective Laser Melting, *Ain Shams Eng. J.*, 2017, **8**, p 475–479

91. Q. Zhao, F. Yang, R. Torrens, and L. Bolzoni, Allotropic Phase Transformation and High-Temperature Tensile Deformation Behaviour of Powder Metallurgy Ti-5553 Alloy, *Int. J. Refract. Met. Hard Mater.*, 2020, **90**, p 1–8

92. H. Schwab, M. Bönisch, L. Giebeler, T. Gustmann, J. Eckert, and U. Kühn, Processing of Ti-5553 with Improved Mechanical Properties via an In-Situ Heat Treatment Combining Selective Laser Melting and Substrate Plate Heating, *Mater. Des.*, 2017, **130**, p 83–89

93. H. Schwab, F. Palm, U. Kühn, and J. Eckert, Microstructure and Mechanical Properties of the Near-Beta Titanium Alloy Ti-5553 Processed by Selective Laser Melting, *Mater. Des.*, 2016, **105**, p 75–80

94. T. Maimaitiyili, K. Mosur, T. Kurzynowski, N. Casati, and H. Van Swygenhoven, Phase Studies of Additively Manufactured Near Beta Titanium Alloy-Ti55511, *Materials*, 2020, **13**, p 1–14

95. M. Malý, C. Höller, M. Skalon, B. Meier, D. Koutný, R. Pichler, C. Sommitsch, and D. Paloušek, Effect of Process Parameters and High-Temperature Preheating on Residual Stress and Relative Density of Ti6Al4V Processed by Selective Laser Melting, *MDPI Mater.*, 2019, **12**, p 1–13

96. H. Carlton, K. Klein, and J. Elmer, Evolution of Microstructure and Mechanical Properties of Selective Laser Melted Ti-5Al-5V-5Mo-3Cr After Heat Treatments, *Sci. Technol. Weld. Join.*, 2019, **24**, p 465–473

97. K. Sankaran and R. Mishra, *Metallurgy and Design of Alloys with Hierarchical Microstructures*, Elsevier, Amsterdam, 2017

98. S. Veek, D. Lee, R. Boyer, and R. Briggs, The Castability of Ti-5553 Alloy, *Adv. Mater. Process.*, 2004, **162**, p 47–49

99. P. Barriobero-Vila, J. Gussone, K. Kelm, J. Haubrich, A. Stark, N. Schell, and G. Requena, An In Situ Investigation of the Deformation Mechanisms in a β-Quenched Ti-5Al-5V-5Mo-3Cr Alloy, *Mater. Sci. Eng.*, 2018, **717**, p 134–143

100. C.G. Rhodes and N.E. Paton, The Influence of Microstructure on Mechanical Properties in Ti-3Al-8V-6Cr-4Mo-4Zr (Beta C), *Metall. Trans.*, 1977, **8A**, p 1749–1761

101. V. Tungala, A. Dutt, D. Choudhuri, J. Mishra, S. Tamirisakandala, K. Cho, and R. Brennan, Friction Stir Processing of Beta C and Ti-185: A Unique Pathway to Engineer Microstructures for Exceptional Properties in β Titanium Alloys, *Metall. Mater. Trans.*, 2019, **50A**, p 4075–4084

102. C. Madikizela, L.A. Cornish, L.H. Chown, and M. Möller, Microstructure and Mechanical Properties of Selective Laser Melted Ti-3Al-8V-6Cr-4Zr-4Mo Compared to Ti-6Al-4V, *Mater. Sci. Eng.*, 2019, **747**, p 225–231

103. M.J. Bermingham, D.H. StJohn, J. Krynen, S. Tedman-Jones, and M.S. Dargusch, Promoting the Columnar to Equiaxed Transition and Grain Refinement of Titanium Alloys during Additive Manufacturing, *Acta Mater.*, 2019, **168**, p 261–274

104. M.J. Bermingham, D. Kent, B. Pace, J.M. Cairney, and M.S. Dargusch, High Strength Heat-Treatable β-Titanium Alloy for Additive Manufacturing, *Mater. Sci. Eng.*, 2020, **791**, p 1–7

105. Z. Zhu, H. Songxiao, Y.E. Wenjun, and Z. Shuqi, Development of Beta Titanium Alloys. *Titanium'99: Science and Technology* (1999)

106. D.M. Berczik, Age Hardenable Beta Titanium Alloy. United States Patent 5,176,762, 5 January 1993

107. S. Zhang, W. Zeng, X. Gao, D. Zhou, and Y. Lai, Role of titanium carbides on microstructural evolution of Ti-35V-15Cr-0.3Si-0.1C alloy during hot working, *J. Alloys Compd.*, 2016, **684**, p 201–210

108. F.S. Sun and E.J. Lavernia, Creep Behavior of Nonburning Ti-35V-15Cr-xC Alloys, *J. Mater. Eng. Perform.*, 2005, **14**, p 784–787

109. X.X. Wang, W.Q. Wang, and Y.Q. Zhang, Effect of Heat Treatment and Thermal Exposure on Microstructure of the Alloy C+ Bars, *Mater. Sci. Forum*, 2013, **765**, p 506–510

110. R.W. Schutz, Environmental Behavior of Beta Titanium Alloys, *J. Miner. Met. Mater. Soc. (TMS)*, 1994, **46**, p 24–29

111. Y. Lai, P. Zhan, X. Zhan, X. Liu, Y. Feng, H. Kou, F. Ma, and W. Zeng, Physical Properties of WSTi3515S Burn-Resistant Titanium Alloy, *Rare Met.*, 2016, **35**, p 361–366

112. Q. Wang, C. Han, T. Choma, Q. Wei, Y. Yan, B. Song, and Y. Shi, Effect of Nb Content on Microstructure, Property and In Vitro Apatite-Forming Capability of Ti-Nb Alloys Fabricated via Selective Laser Melting, *Mater. Des.*, 2017, **126**, p 268–277

113. J.C. Wang, Y.J. Liu, P. Qin, S.X. Liang, T.B. Sercombe, and L.C. Zhang, Selective Laser Melting of Ti-35Nb Composite from Elemental Powder Mixture: Microstructure, Mechanical Behavior and Corrosion Behavior, *Mater. Sci. Eng. A*, 2019, **760**, p 214–224

114. H. Schwab, K.G. Prashanth, L. Löber, U. Kühn, and J. Eckert, Selective Laser Melting of Ti-45Nb Alloy, *Metals*, 2015, **5**, p 686–694

115. J.P. Luo, Y.J. Huang, J.Y. Xu, J.F. Sun, M.S. Dargusch, C.H. Hou, L. Ren, R.Z. Wang, T. Ebel, and M. Yan, Additively Manufactured Biomedical Ti-Nb-Ta-Zr Lattices with Tunable Young's Modulus: Mechanical Property, Biocompatibility, and Proteomics Analysis, *Mater. Sci. Eng. C*, 2020, **114**, p 1–16

116. L. Zhou, T. Yuan, R. Li, J. Tang, M. Wang, and F. Mei, Anisotropic Mechanical Behavior of Biomedical Ti-13Nb-13Zr Alloy Manufactured by Selective Laser Melting, *J. Alloys Compd.*, 2018, **762**, p 289–300

117. L. Zhou, T. Yuan, J. Tang, L. Li, F. Mei, and R. Li, Texture Evolution, Phase Transformation and Mechanical Properties of Selective Laser Melted Ti-13Nb-13Zr, *Mater. Charact.*, 2018, **145**, p 185–195

118. R. Lisboa, W. Capute, L. Deng, T. Gustmann, S. Pauly, C. Shyinti, and P. Gargarella, Processing a Biocompatible Ti–35Nb–7Zr–5Ta Alloy by Selective Laser Melting, *J. Mater. Res.*, 2020, **35**, p 1143–1153

119. X. Cheng, S. Liu, C. Chen, W. Chen, M. Liu, R. Li, X. Zhang, and K. Zhou, Microstructure and Mechanical Properties of Additive Manufactured Porous Ti-33Nb-4Sn Scaffolds for Orthopaedic Applications, *J. Mater. Sci. Mater. Med.*, 2019, **30**, p 1–12

120. Y. Li, Y. Ding, K. Munir, J. Lin, M. Brandt, A. Atrens, Y. Xiao, J.R. Kanwar, and C. Wen, Novel β-Ti35Zr28Nb Alloy Scaffolds Manufactured Using Selective Laser Melting for Bone Implant Applications, *Acta Biomater.*, 2019, **87**, p 273–284

121. R. Ummethala, P. Karamched, S. Rathinavelu, N. Singh, A. Aggarwal, K. Sun, E. Ivanov, L. Kollo, I. Okulov, J. Eckert, and K.G. Prashanth, Selective Laser Melting of High-Strength, Low-Modulus Ti–35Nb–7Zr–5Ta Alloy, *Materialia*, 2020, **14**, p 1–9

122. Y.J. Liu, Y.S. Zhang, and L.C. Zhang, Transformation-Induced Plasticity and High Strength in Beta Titanium Alloy Manufactured by Selective Laser Melting, *Materialia*, 2019, **6**, p 1–5

123. N. Hafeez, J. Liu, L. Wang, D. Wei, Y. Tang, W. Lu, and L.C. Zhang, Superelastic Response of Low-Modulus Porous Beta-Type Ti-35Nb-2Ta-3Zr Alloy Fabricated by Laser Powder Bed Fusion, *Addit. Manuf.*, 2020, **34**, p 1–9

124. J. Wang, Y. Liu, C.D. Rabadia, S.X. Liang, T.B. Sercombe, and L.C. Zhang, Microstructural Homogeneity and Mechanical Behavior of a Selective Laser Melted Ti-35Nb Alloy Produced from an Elemental Powder Mixture, *J. Mater. Sci. Technol.*, 2021, **61**, p 221–233

125. C.A. Biffi, A.G. Demir, M. Coduri, B. Previtali, and A. Tuissi, Laves Phases in Selective Laser Melted TiCr1.78 Alloys for Hydrogen Storage, *Mater. Lett.*, 2018, **226**, p 71–74